UCLA

UCLA Electronic Theses and Dissertations

Title

Photonic Control of Thermal Infrared Radiation

Permalink

https://escholarship.org/uc/item/09c710zm

Author

Brewer, John Benjamin

Publication Date

2023

Peer reviewed|Thesis/dissertation

eScholarship.org Powered by the California Digital Library
University of California

UNIVERSITY OF CALIFORNIA
Los Angeles

Photonic Control of Thermal Infrared Radiation

A dissertation submitted in partial satisfaction
of the requirements for the degree
Doctor of Philosophy in Materials Science and Engineering

by

John Benjamin Brewer

2023

© Copyright by
John Benjamin Brewer
2023

ABSTRACT OF THE DISSERTATION

Photonic Control of Thermal Infrared Radiation

by

John Benjamin Brewer
Doctor of Philosophy in Materials Science and Engineering
University of California, Los Angeles, 2023
Professor Aaswath Pattabhi Raman, Chair

Thermal infrared radiation, conventionally defined as the band from 7-14 μm, is an important waveband for a variety of applications in radiative cooling and thermal imaging. Due to its broadband character, traditional resonant photonic phenomena's typically extremely narrow band, high quality factor behaviors are not generally applied to the thermal wavelengths. Here we show a variety of ways in which conventionally high quality factor, narrow band resonances can be augmented for effective use over broadband regimes. This theme is demonstrated in the cases of relativistic lightsails, thermal infrared optics, and solar cell module glass. I show how conventional nanophotonic structures can be applied to these systems to derive benefits such as improved radiative cooling performance, increased interfacial transmission efficiency, and increased photovoltaic module power generation efficiency and longevity.

The dissertation of John Benjamin Brewer is approved.

Artur R. Davoyan

Yang Yang

Ya-hong Xie

Aaswath Pattabhi Raman, Committee Chair

University of California, Los Angeles

2023

To those who believed in my potential
when I did not

TABLE OF CONTENTS

1 Introduction **1**

2 Multi-scale photonic emissivity engineering for relativistic lightsail thermal regulation **3**

- 2.1 Challenges 3
- 2.2 Background 4
- 2.3 Design: Materials and Geometry 6
- 2.4 Simulations and Acceleration Optimization 7
- 2.5 Thermal Considerations 10
- 2.6 Multiscale Mie Resonance Structure 11
- 2.7 Supporting Information 17
  - 2.7.1 Thermal Limit 20
  - 2.7.2 Payload Mass Effect 20
  - 2.7.3 Form of $h(\beta)$ and influence on design 20
  - 2.7.4 Alternative form of acceleration vs. temperature plot 21
  - 2.7.5 Form of the Power Balance Equation 21
  - 2.7.6 Acceleration Distance Comparison of Mie Structure Vs. Continuous Structure 23
  - 2.7.7 Connected Mie Resonant Structure 23
- 2.8 Opto-Mechanical Modeling assistance 24

3 Resonant Anti-Reflection Metasurfaces for Infrared Transmission Optics **26**

- 3.1 Background 26
- 3.2 Design: Materials and Simulation 29
- 3.3 Transmission and Imaging Characteristics 35
- 3.4 Supporting Information 41

3.4.1 Materials and Methods 41
3.4.2 Supplemental Field Plots 43
3.4.3 Experimental setup of MTF Measurement 44
3.4.4 MTF difference between system with windows and stock system . . . 46
3.4.5 Angular Spectra Comparison 47
3.4.6 Front to Back Pattern Misalignment Study 48
3.4.7 Qualitative comparison of AR approaches and materials 49
3.4.8 Acknowledgement 50

4 Resonant surface engineering for photovoltaic cell front glass improvement 51

4.1 Background 51
4.2 Design and Simulation Landscape 52
4.3 Fabrication 54
4.4 Measurement and Results 56

5 Conclusions and Future Work 58

LIST OF FIGURES

2.1 BSI sail design. (a) Schematic diagram demonstrating relevant optical considerations for an accelerating lightsail (b) Section of sail with hole diameter to period ratio of 90% (c) Front and side view of single design period. (d) Enlarged view of multilayer structure. Yellow regions represent Si_3N_4 while green regions represent MoS_2. 5

2.2 Reflective properties of multilayer photonic sail structures. (a) Color maps of minimum acceleration distance designs for a 1 g payload as a function of the most sensitive geometric parameters. Each color map represents a two parameter slice of the five parameter design space composed of the period/lattice constant, the hole diameter-to-period ratio, and the thicknesses of each of the three layers. Tile colormap shows the acceleration distance for the design specified by the parameter values on the axis, sliced at top and bottom Si_3N_4 layer thicknesses of 5 nm, the optimal values to minimize acceleration. Outlined tiles marked with the red "×" show the parameter values of the lowest acceleration distance design in our simulation space. (b) Dependence of lowest acceleration distance sail reflection spectra on payload mass over the Doppler-shifted laser wavelength range. Lower mass payloads reward reductions in the sail mass more than increases in the sail's integrated reflection spectra. (c) Demonstration of spectral perturbation due to the addition of lower index, high emissivity Si_3N_4 layers. Insets provide schematic diagrams of sail designs corresponding to plot colors. 8

2.3 Emissive properties of multilayer photonic sail structures for a 1 g payload. (a) Minimum acceleration distance as a function of temperature for three imposed values of sail material extinction coefficient. The vertical black dotted line marks the defined ultra-high vacuum thermal limit. On the central curve ($\kappa = 10^{-7}$) the blue point and accompanying line mark the acceleration distance and temperature of the TEAM design. The TEAM design is that which obtains the TEAM distance, i.e., that which has the shortest acceleration distance among those design alternatives whose temperatures do not exceed the thermal limit. The red dotted line marks the minimum acceleration distance achievable in our design space, and demonstrates that the corresponding design has a peak temperature > 5000 K for $\kappa = 10^{-7}$, meaning the corresponding red point is not visible. The solid red curve corresponds to a simulated value of $\kappa = 10^{-8}$, which shows a solution below 5000 K, but it is still more than double the enforced thermal limit. Decreasing κ has the effect of decreasing the TEAM distance from 23.3 Gm to 11.4 Gm. (b) Comparison of the hemispherical emissivity spectra, i.e. the direction-averaged spectral emissivity, of the simple acceleration merited design corresponding to the off plot red point in (a) vs. acceleration-temperature co-merited design corresponding to blue point in (a). Calculated maximum temperatures of the designs are also provided. (c) Plot showing thermally endurable acceleration minimum (TEAM) distance for six selected values of κ, connected to show trended behavior. Values of κ greater than the plot range have no solution within our simulated sail set, meaning layers of Si_3N_4 thicker than 110nm are necessary to maintain thermal integrity of the sail in flight. 12

2.4 (a) Mie resonant enhancement schematic diagram illustrating the proposed multi-scale Mie resonator design. The green strips show the possibility of scaffolds used to support the Mie resonator structure. (b) Spatial absorption profiles of Mie resonances in (c) corresponding to the respectively labelled spectral peaks. (c) Hemispherical exitance of Mie resonant structure vs. conventional photonic crystal structure, calculated at a temperature of 1000 K, demonstrating a pathway for possible emissivity enhancement. (d) Demonstration of spectrally integrated hemispherical exitance enhancement as a function of temperature. 15

2.5 Demonstration of correlation between payload mass and acceleration distance. Each gram of mass adds approximately 4 Gm of acceleration distance to the system. 21

2.6 Simple plot of $h\beta$ function showing its monotonic increasing behavior, demonstrating that reflectivity at higher velocities is weighted more heavily then reflectivity at lower velocities 22

2.7 Plot of $h\beta$ function showing its monotonic increasing behavior, demonstrating that reflectivity at higher velocities is weighted more heavily then reflectivity at lower velocities 23

2.8 Continuous Mie structure design. The black outlines serve to highlight the positions of the Mie resonant features against the continuous reflective green layer, but would not exist in the actual design. 24

3.1 A schematic comparison of anti-reflection for a) Absorption enhancement: In this case, waves enter the substrate but do not leave it, being absorbed either as heat or generating photocurrent. As they are not exiting, their output state is disregarded. b) Non-image preserving transmission enhancement: In this case, waves enter the substrate and are scattered by either or both of the front and rear surfaces. This configuration could occur in a multijunction cell, or any diffuser optic. c) Image preserving transmission enhancement. In this case, the shape of the incoming wave is preserved as it exits the substrate optic. Input plane waves exit as plane waves, and waves with more complex wave fronts will be maintained with an added phase due to propagation. 30

3.2 a) Pictorial schematic of a single hexagonal unit cell of finalized design. Design is patterned on both sides of wafer. $d = 1.5\ \mu m$, $h = 1.2\ \mu m$, $a = 2.0\ \mu m$, resulting in a critical trench feature size of 0.5 μm. Plane cross section through unit cell depicted in b is shown. b) E-field component plots for normal and 30° incidence. Simulation cross-section at $9.6\mu m$ for a truncated $16\mu m$ thick substrate to demonstrate plane-wave propagation, shown for P and S polarizations. c) Comparison of simulated spectral transmission for unpolarized light at normal and 30° incidence. At least a 20% uplift over the entire band and 0°-30° angular range. d) Slice of simulation parameter sweep for optimal $1.2\mu m$ cylindrical pillar feature height, showing trench width vs. period multiplier. Period for a given tile is calculated by multiplying x and y positions for that tile. Feature width can then be calculated by subtracting the y value from the resulting period. 34

3.3 a) SEM image of surface patterning, which is present on both sides of substrate. b) Imaging test of fabricated optic taken on FLIR BOSON+ thermal camera. Borders to patterned region and wafer edge have been added for clarity, Si transmission improvement is immediately noticeable compared to unpatterned edges of wafer, and compares favorably with the Ge window on the left. c) Comparison of unpatterned (black) and patterned (blue) intrinsic Si, and AR coated Ge (yellow) windows at 0° incidence. Patterning results in an up to 40% increase in transmission over the bare case. d)Angular falloff plot showing integrated spectral transmission over the 7-14μm band for bare Si, BBAR coated Ge window, and Mie patterned Si. 36

3.4 Modulation transfer function (MTF) comparison between control LWIR optical system, Ge window optic, and Mie-resonant high transmission Si a) On-axis, b) at 10° or 70% field, and c) at 14° or 93% horizontal field. MTF values are comparable between all 3 systems at all field angles, indicating that scattering from surface does not cause significant imaging performance loss. To highlight the relative magnitudes of the curves more clearly, a zoomed inset has been included in 4b, reflecting that the MTF presents as higher with additional optics, which we note is likely an artifact resulting from spectral filtering occurring from the added optics. Camera used was FLIR BOSON+, 640 x 512 pixel camera with 12 μm pixel pitch. Spatial frequency data was plotted out to detector Nyquist frequency of $41.\bar{6}$ lp/mm. 38

3.5 Tranverse plane field plots of Mie-Resonant AR structure at normal incidence, with structure boundaries indicated by black circles. E_z and H_z dipole resonances overlaps are visible in the rightmost column. Note that each plot has been range normalized to show greatest contrast. 43

3.6 Picture of experimental setup. Camera and optic rotate together on stage for MTF measurements, to simulate window being a part of lens optical stack. . . . 45

3.7 Difference between system with added Ge window and stock system (yellow) and system with Si window added and stock system (blue) at each measured spatial frequency a) On axis b.) at 10 degrees and c.) at 14 degrees. 46

3.8 Angular spectra measurements for a)bare silicon b)Mie-resonant silicon and c) BBAR coated Germanium window optic. 47

3.9 Angular spectra measurements for varying degrees of misalignment at 0°, 15°, 30°, 45°, and 60° incidence angles (columns) for S and P polarizations (rows). Note that all lines are overlapping, so only fully out of phase misalignment color is visible. This is confirmed by the 60° simulations, which show slight divergence at low wavelengths. 48

4.1 a) Pictorial schematic of a single square unit cell cross-section at the top surface of a pane of module glass. Design consists of a silica spacer layer in which is embedded a lower index Si_3N_4 resonator layer followed by a higher index, offset Ta_2O_5 resonator layer, and finally topped with an aerogel anti-reflective layer. b) Simulated performance of optimal design. c) Design E-fields for S and P polarizations, taken at the cross-section shown in a and the peak position noted in b. 53

4.2 Optimization landscape diagrams of seven different design classes. Two layer resonator designs are shown in the top row, while single resonator layer designs are shown in the bottom row. The meaning of the x-axis value is given by eq. 4.2, while the meaning of the y-axis value is given by eq. 4.3. The black point and corresponding vertical and horizontal line mark the merit position of untreated glass. The goal is to isolate designs which fall in the upper right quadrant with respect to this bare glass "origin". Note that the conventional photonic crystal slab (PhC) designs contain no valid solutions in this quadrant. 54

4.3 Fabrication outline of patterned glass on fused silica substrate. The final step which was not performed for the initial samples consists of a 120nm aerogel AR coating to assist with visible wavelength transmission efficiency. 55

4.4 a) A representative example design consisting of an Si_3N_4 resonator layer encapsulated in an SiO_2 matrix. Actual resonator cross-section shape is shown in each plot inset, presented with geometric parameters. b) Measured reflectance of 8 proof of concept designs, compared to bare, unpatterned glass. 56

LIST OF TABLES

3.1 A brief qualitative comparison table for the AR approaches covered within the work. Asterisk denotes that under normal conditions adhesion is very good, but large thermal swings can cause delamination, as covered in the main text. 49

3.2 A brief qualitative comparison table for the material systems covered within the work. 50

ACKNOWLEDGMENTS

Chapter 2 is a version of: Brewer, J. et al. Multiscale Photonic Emissivity Engineering for Relativistic Lightsail Thermal Regulation. Nano Lett. 22, 594–601 (2022). Campbell, M. proofread and revised work, provided mechanical engineering expertise, and confirmed derivations. Kumar, P. proofread and revised work, provided materials growth and fabrication expertise, and guided materials candidate selection. Kulkarni, S aided with optical simulations. Jariwala, D and Bargatin, I and Raman, A.P. were all co-P.I.s

Chapter 2 section 2.8 makes reference to a companion work: Campbell, M. F., Brewer, J., Jariwala, D., Raman, A. P. & Bargatin, I. Relativistic Light Sails Need to Billow. Nano Lett. 22, 90-96 (2022).

Chapter 3 is a version of: Brewer, J., Kulkarni, S. & Raman, A. P. Resonant Anti-Reflection Metasurfaces for Infrared Transmission Optics. Nano Lett. 23, 8940-8946 (2023). Kulkarni S. Aided with simulations and experimental image capture. Raman A.P. was P.I.

Funded in part by:
National Science Foundation Graduate Fellowship Research Program
UCLA NRT-INFEWS

Special thanks to:
UCLA Nanolab Cleanroom Facilities
UCLA Hoffman2 Computational Cluster

VITA

2016–2018	Undergraduate researcher, University of Arizona, Tucson, Arizona. Processed samples in cleanroom using sputter deposition, electron beam evaporation, and reactive ion etching techniques
2018	Undergraduate intern, Airy Optics, Tucson, Arizona. Gained general knowledge of and created documentation for Polaris-M software functions.
2018	B.S. (Optical Sciences and Engineering, Minors: Mathematics, Materials Science and Engineering) University of Arizona, Tucson, Arizona.
2018	Graduate Technical Intern, Intel Corporation, Phoenix, Arizona.
2018–present	Ph.D. Candidate (Materials Science and Engineering) UCLA, Los Angeles, California.

PUBLICATIONS

Brewer, J., Kulkarni, S. & Raman, A. P. Resonant Anti-Reflection Metasurfaces for Infrared Transmission Optics. Nano Lett. (2023).

Brewer, J. et al. Multiscale Photonic Emissivity Engineering for Relativistic Lightsail Thermal Regulation. Nano Lett. 22, 594–601 (2022).

Campbell, M. F., Brewer, J., Jariwala, D., Raman, A. P. & Bargatin, I. Relativistic Light Sails Need to Billow. Nano Lett. 22, 90-96 (2022).

CHAPTER 1

Introduction

Engineering methods of manipulating electromagnetic radiation has been a central theme of physics for hundreds of years. The study of thermal radiation has been a particularly influential part of physics history, where the investigation of blackbodies and the resulting ultraviolet catastrophe ultimately led to Einstein's theory of the quantum nature of light. Blackbody radiation, and therefore EM waves, exist all throughout the universe because all massive bodies are at some finite temperature. The thermal signatures of Earth and terrestrial objects are of particular interest to humanity for obvious reasons. Earth is at an average temperature of 20 $°C$ or around 293 K, and using Wein's displacements law, its blackbody spectrum peak can be determined as approximately 13 μm. For this reason, the thermal infrared band is conventionally defined to be from 7-14 μm which captures the blackbody peaks of objects up to $270°C$.

Technologies such as passive radiative coolers and thermal imagers, which operate in or leverage this waveband, have evolved immensely as microfabrication techniques have matured. These recent technological leaps have given rise to an exciting advancements in the field of thermal optics. This in turn has resulted in many opportunities to combine existing knowledge with new techniques and fabrication limits in order to create novel optical designs. In the proceeding pages, I will be describing my work in developing several such designs. These devices combine resonant phenomena in photonics generally employed for spectrally narrow applications (i.e. less than 50 nm), and expands them for use over the broadband thermal infrared band.

Resonances occur when a periodic perturbation aligns with the natural frequency of a physical system. In the context of optics, this can occur when an object's physical properties overlap with a given wavelength of light, such as the plasma frequency, or when the geometric shape and size of a material with the correct physical properties is excited. This latter case is investigated by the field known as metamaterials or meta-optics. One subset of meta-optics specifically investigates so called "all-dielectric" systems, which are of interested due to their intrisically low loss as compared to plasmonic metamaterial systems, and high performance in optical regimes. These all-dielectric Mie-resonances are heavily predicated on the use of high-index low loss optical materials, and rely on specific geometries to induce resonant behaviors that can result in a variety of useful optical functionalities. By tuning the geometries and materials in these devices, resonances can be combined or broadened to allow for functionality over thermal bandwidths.

In this work, I will demonstrate how this class of broadband resonance phenomena can be leveraged for a variety of applications in radiative cooling, thermal imaging, and photovoltaic improvement.

CHAPTER 2

Multi-scale photonic emissivity engineering for relativistic lightsail thermal regulation

The Breakthrough Starshot Initiative aims to send a gram-scale probe to Proxima Centuri B using a laser-accelerated lightsail traveling at relativistic speeds. Thermal management is a key lightsail design objective because of the intense laser powers required but has generally been considered secondary to accelerative performance. Here, we demonstrate nanophotonic photonic crystal slab reflectors composed of 2H-phase molybdenum disulfide and crystalline silicon nitride, highlight the inverse relationship between the thermal band extinction coefficient and the lightsail's maximum temperature, and examine the trade-off between minimizing acceleration distance and setting realistic sail thermal limits, ultimately realizing a thermally endurable acceleration minimum distance of 23.3 Gm. We additionally demonstrate multi-scale photonic structures featuring thermal-wavelength-scale Mie resonant geometries and characterize their broadband Mie resonance-driven emissivity enhancement and acceleration distance reduction. More broadly, our results highlight new possibilities for simultaneously controlling optical and thermal response over broad wavelength ranges in ultralight nanophotonic structures.

2.1 Challenges

Interstellar travel is a fundamental scientific and engineering challenge currently beyond the capacity of advanced nuclear pulse[1] and fusion power-based[2–4] engines. An alternative approach proposed by the Breakthrough Starshot Initiative entails a laser-propelled lightsail carrying a gram-scale probe at relativistic speeds to visit Earth's nearest candidate habitable exoplanet, Proxima Centauri B[5–7] within twenty years. Lightsails are ultra-lightweight, highly reflective surfaces propelled via photon momentum transfer[8], and are central to this remarkable potential capability.

Lightsail-driven vehicles have been extensively studied for solar[9–12], astrophysical[13,14], and laser[15–18] sources. In the final case, relativistic lightsail design and material selection faces an extreme set of demands due to the target velocity requiring the use of gigawatt-scale light irradiances on the sail. The high laser irradiances in turn impose strong material, mechanical, and optical constraints for functional sail design[19]. Accelerative performance necessitates high broadband reflectivity to accelerate the sail and payload to its target velocity as quickly as possible, and to account for red-shifting due to the relativistic velocities involved. In addition, sail mass should be minimized, and sail shape[20] or patterning[21] should result in stable beam riding even when faced with non-ideal beam shapes or alignments[22]. Sail survivability motivates the need for sufficient mechanical robustness to survive both extreme acceleration-induced forces and interaction with the interstellar medium[23–25]. Finally, survivability requires vanishingly small absorptivities over the red-shifted laser band to prevent excessive heating, as well as sufficient emissivity to radiatively dissipate heat generated by any residual laser band absorptivity. Solutions to these criteria have only recently come within reach through advances in nanofabrication[26–28], radiative cooling[29,30], and nanophotonics[31–34].

2.2 Background

Pioneering work on relativistic lightsails[19] has examined aspects such as passive beam-riding stability[21,35,36] and maximizing reflectivity on a per-mass basis[37,38] in sails composed primarily of Si, SiO_2[21,35,37,38], and Si_3N_4[38,39]. In these works, the sail's temperature has largely been a secondary consideration rather than a primary target to be minimized. Here, we propose a method to select sail designs by co-optimizing both their thermal performance and reflectivity, and explore for the first time the use of MoS_2 as a highly reflective material for photonic lightsails. Furthermore, we demonstrate a multi-scale photonic structure that simultaneously optimizes for acceleration distance and enhances thermal emissivity to reduce sail temperatures.

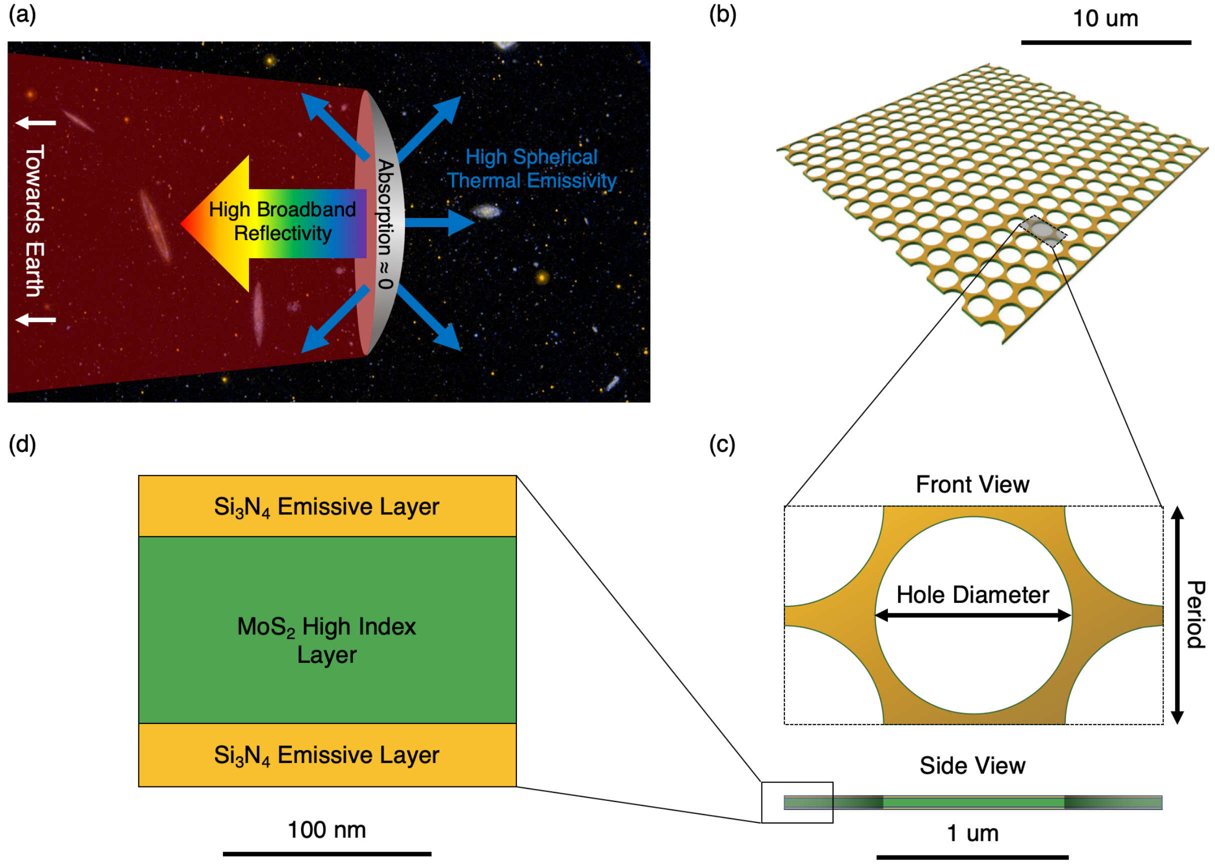
(a)
Towards Earth
High Broadband Reflectivity
Absorption ≈ 0
High Spherical Thermal Emissivity
(b)
10 um
(d)
Si_3N_4 Emissive Layer
MoS_2 High Index Layer
Si_3N_4 Emissive Layer
100 nm
(c)
Front View
Hole Diameter
Period
Side View
1 um

Figure 2.1: BSI sail design. (a) Schematic diagram demonstrating relevant optical considerations for an accelerating lightsail (b) Section of sail with hole diameter to period ratio of 90% (c) Front and side view of single design period. (d) Enlarged view of multilayer structure. Yellow regions represent Si_3N_4 while green regions represent MoS_2.

2.3 Design: Materials and Geometry

Our lightsail design is based on a multilayer 2D photonic crystal slab-based geometry that features a molybdenum disulfide (MoS_2) reflective core layer surrounded on both sides by silicon nitride (Si_3N_4) emissive layers. Figure 2.1a illustrates the general optical considerations of lightsail design, while Figures 2.1b, c, and d show the geometric parameters we investigated in our periodic concept sails. While previous work has discussed the possible use of MoS_2 for laser-driven lightsails[19], its use in photonic sail designs is still unexplored. Other materials such as diamond and silicon have been suggested but pose challenges due to high vacuum phase instability[40], thermal[41] or stress[42] based band narrowing effects, or surface states[43–45], all of which could cause absorption.

We chose to investigate designs employing MoS_2 for four key reasons. The first is its high refractive index in the Doppler-shifted laser band, ranging from $n = 3.73 - 3.66$, making it a desirable reflective material. Second, its high bandgap energy gives headroom for thermal bandgap narrowing effects that can increase laser absorptivity[46,47]. Third, monolayer grown MoS_2 samples demonstrate zero absorption in the laser bandwidth within ellipsometric measurement limits[48]. Finally, large area monolayer samples have been fabricated successfully, a significant step toward future lightsail-scale films[49–51]. Si_3N_4 has also been recently investigated for lightsails[38,39,52] and remains a promising candidate due to its mature fabricability, low density, and high decomposition temperatures[53,54]. Recent work has demonstrated LPCVD-grown material absorption coefficients of order 10^{-4} cm^{-1}, a value currently limited by the presence of microvoids and hydrogen impurities[55]. Furthermore, Si_3N_4 has intrinsic emissivity characteristics in the 5-14 μm wavelength range[56] that match well with the sail's nominal operating temperature of 500-1000 K.

We employ a tri-layer composite sandwich structure which provides high reflectivity in a lightweight and thermally robust package due to the core MoS_2 layer's superior ratio of refractive index to mass and the sail's large emissive area for cooling from the two Si_3N_4 face layers. In addition to the mass reduction benefits, our design provides reflective enhancement through coupling to broadband guided modes, building on conventional photonic crystal slab theory[32]. While we used this as the basis of our design, the extreme performance required of the lightsail necessitates departures from typical photonic crystal reflectors. Previous nanoscale photonic crystal reflectors in the literature have not been designed specifically for the severe mass constraints, large laser bandwidth, and optimized thermal emissivity that are required for the intended lightsail mission. Finally, our design is fully connected and requires no additional substrate to function as a standalone sail, offering an important structural advantage. However, a large corrugated support backbone may be necessary in practice to help the sail withstand extreme accelerative forces[57]. This structure would provide macroscale sail curvature to increase stability and mechanical robustness[20] while additionally limiting crack propagation in our proposed designs due to patterned hole-induced stress concentrations.

2.4 Simulations and Acceleration Optimization

To benchmark sail designs, we assumed typical design parameters for Breakthrough Starshot: a uniform I = 10 $\frac{\mathrm{GW}}{\mathrm{m}^2}$ laser irradiance on the sail, a laser output wavelength of $\lambda = 1.2\ \mu$m, a 10 m^2 sail area, and a 1 g chip payload mass unless otherwise stated. The acceleration distance figure of merit, as defined by Jin et al.[38] is:

$$D = \frac{c^3}{2I}(\rho_{payload} + \rho_{sail}) \int_0^{0.2} \frac{h(\beta)}{R(\lambda(\beta))} d\beta \tag{2.1}$$

where $h(\beta) = \frac{\beta}{(1-\beta)^2\sqrt{1-\beta^2}}$, I is the laser irradiance in $\frac{\mathrm{W}}{\mathrm{m}^2}$, ρ is areal density in $\frac{\mathrm{kg}}{\mathrm{m}^2}$ (discussed more below), β is the unitless relative velocity (to the speed of light), and $R(\lambda(\beta))$ is the spectral reflectance over the Doppler-shifted laser band. It is worth noting that a constant irradiance term with respect to β implies the use of laser power throttling to ensure the incident power on the sail remains constant throughout its acceleration. A detailed explanation of this can be found in the Supporting Information of Campbell et al.[20]

Optimizing the period and hole diameter of the patterned holes allows for high transmis-

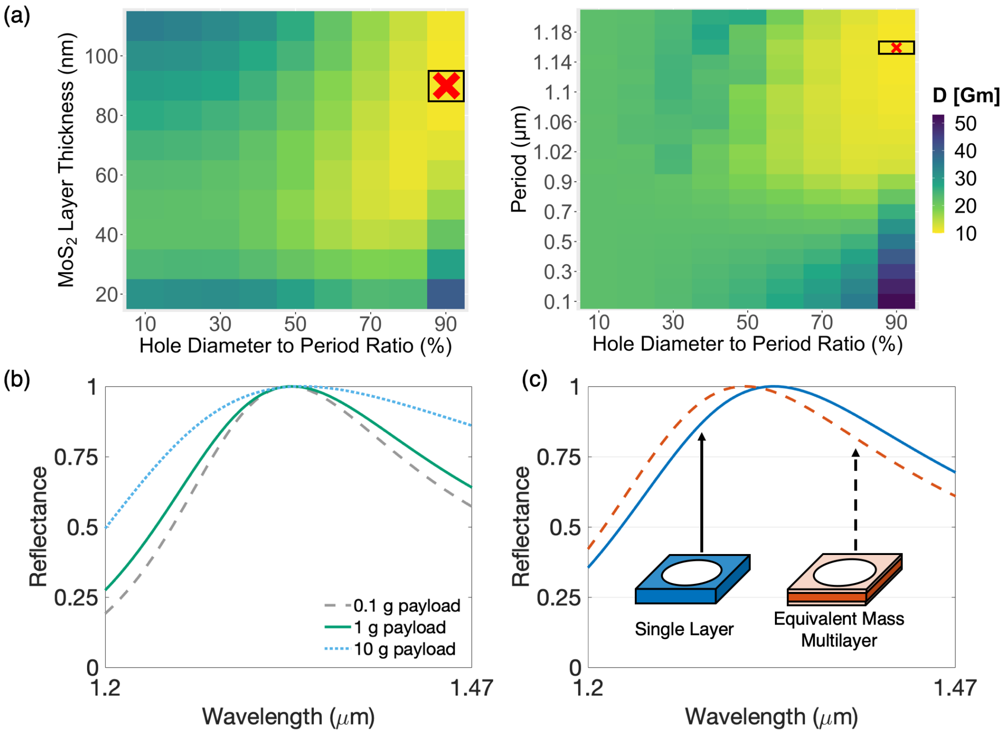

Figure 2.2: Reflective properties of multilayer photonic sail structures. (a) Color maps of minimum acceleration distance designs for a 1 g payload as a function of the most sensitive geometric parameters. Each color map represents a two parameter slice of the five parameter design space composed of the period/lattice constant, the hole diameter-to-period ratio, and the thicknesses of each of the three layers. Tile colormap shows the acceleration distance for the design specified by the parameter values on the axis, sliced at top and bottom Si_3N_4 layer thicknesses of 5 nm, the optimal values to minimize acceleration. Outlined tiles marked with the red "×" show the parameter values of the lowest acceleration distance design in our simulation space. (b) Dependence of lowest acceleration distance sail reflection spectra on payload mass over the Doppler-shifted laser wavelength range. Lower mass payloads reward reductions in the sail mass more than increases in the sail's integrated reflection spectra. (c) Demonstration of spectral perturbation due to the addition of lower index, high emissivity Si_3N_4 layers. Insets provide schematic diagrams of sail designs corresponding to plot colors.

sion and reflection bands of varying spectral bandwidth[32]. Figures 2.2a and b demonstrate the dependence of acceleration distance on key design parameters in our sail design space. Our optimal acceleration distance merited design has a period of 1.16 μm, a hole period to diameter ratio of 90%, 5 nm thick emissive Si_3N_4 layers, and a 90 nm thick MoS_2 reflective core, placing it in a regime of very low thickness values relative to the lattice constant, $< 0.1a$. Thinning of the high-index core maintains access to broadband Fabry-Perot-like reflection modes at normal incidence with the added effect of minimizing the overall sail mass. This demonstrates the broad range of possible acceleration distance values that our design space encompasses.

The precise payload chip mass, though likely to be roughly 1 g, has not yet been determined for the actual craft, such that understanding the effect of mass on our optimal design is critical. Note that payload mass can be converted to the areal density value shown in (2.1) according to $\rho_{payload} = m_{payload}/A_{sail}$. Figure 2.2b plots the laser band reflection spectra of the lowest acceleration distance design for three payload masses, demonstrating that as the payload mass decreases, reducing the sail's mass is rewarded more than improving its reflectance spectrum. This means that sail mass becomes a stronger consideration when the payload mass is small. A further analysis showing the minimum acceleration distance vs. payload mass can be found in the Supporting Information, which is corroborated by results in Jin et al.[38]

The Si_3N_4 layers we have introduced are necessary to enhance thermal emissivity; however, these can also have the effect of shifting the peak of the sail reflection spectra to lower wavelengths compared to single-layer MoS_2-only designs, as shown in Figure 2.2c. The shift results in a $\sim 6\%$ increase in the acceleration distance figure of merit due to the monotonically increasing nature of $h(\beta)$ in (2.1). This highlights that having high reflectivity at longer Doppler-shifted laser band wavelengths is more beneficial then at shorter wavelengths given a constant irradiance on the sail. We note that since the designs shown in Figure 2.2c have identical masses of $\sim 1.3\ g$, this effect is attributable to the change in the refractive index profile alone.

Our simulated sail design set resulted in an optimal reflective design with an acceleration distance of 10.6 Gm when carrying a 1 g payload, comparable in performance to current leading designs[38]. Importantly, our methodology takes into account all mass required for acceleration and cooling and our design does not require a connecting support structure. If necessary, adding a 1 g mechanical backbone would provide additional structural stability and increase the acceleration distance to 15.2 Gm. Furthermore, the geometry of this design is not computationally optimized, and optimization could yield still lower acceleration distances. While the current design is competitive with the best shown previously[38], we will show that adding realistic thermal considerations increases acceleration distances by 120%.

2.5 Thermal Considerations

Lightsails can easily disintegrate during acceleration, making sail integrity just as critical as reflection-driven performance metrics. While the sail must exhibit extremely low absorptivity, this value is finite in practice and the sail's temperature will increase due to the high incident laser irradiance. Interaction with the interstellar medium at relativistic speeds could also cause heating[23]. Additionally, the sail's component materials can become more absorptive as their temperature rises, raising concerns about thermal runaway[58] and increasing the probability of sail thermal failure. Our approach seeks to optimize sail design in terms of its acceleration characteristics while ensuring sufficient radiative cooling characteristics to maintain sail integrity. We adopt the ultra-high vacuum (UHV) sublimation temperature $T_{sublimation}$ of the sail materials as a thermal limit. Note that since the UHV sublimation temperature is less than the 1 atm melting temperature selected as the thermal limit in other recent lightsail studies[21,35], this represents a conservative design decision. In our case, we adopted $T_{limit} = T_{sublimation,\mathrm{MoS_2}} \sim 1000$ K, which is the lower UHV sublimation point among the two materials used[59,60] (see Supporting Information).

To our knowledge, the temperature dependent absorption properties of MoS_2 have only been investigated in the Doppler-shifted laser band up to 500 K using ellipsometric methods[61]. This initial data suggests that the absorptivity of MoS_2 as a function of temperature may actually decrease while its refractive index stays relatively constant, even in the presence of thermally activated band narrowing. Investigation at higher temperatures with higher sensitivity will be necessary to fully determine thermal runaway-based effects. We further note that ellipsometric methods, which were used to generate the optical constant data in our simulations, cannot reliably measure absorptivities of less than 1% of the incoming source intensity. This strongly highlights the need for sensitive measurements for qualification of materials used for relativistics lightsails using techniques such as photothermal deflection[62] and photocurrent[63] spectroscopy. New growth methods such as chemical vapor transport and self-flux growth[64–66] offer the possibility of producing electronically thick bulk film samples having optical quality comparable to or better than the lowest values reported in the optical constant dataset used for simulation and analysis in this work[48].

We implicitly calculated the maximum temperature T_{max} reached by each sail in our space of over 3×10^5 designs using the following equation:

$$P_{sail}\alpha_{sail} = 2A_{sail}\int_a^b \frac{c_1}{\lambda^5} \cdot \frac{\epsilon_{sail}(\lambda)}{e^{\frac{c_2}{\lambda T_{max}}} - 1} d\lambda \tag{2.2}$$

where P_{sail} is the incident laser power on the sail, α is the laser band spectrally averaged integrated absorptivity of the sail, A_{sail} is the area of a single side of the sail, the factor of two accounts for the emission by Si_3N_4 on both sides of the sail, $a = 1.55$ μm, $b = 14.05$ μm, $c_1 = 2\pi hc^2$, $c_2 = hc/k_b$, h is Planck's constant, c is the speed of light, k_b is Boltzmann's constant, and ϵ_{sail} is the spectral sail emissivity (see Supporting Information).

2.6 Multiscale Mie Resonance Structure

Our initial designs leveraging conventional photonic crystal theory have desirable properties from an acceleration merit standpoint, but their thermal band radiant exitance is highly dependent on the intrinsic spectral emissivity of their component materials. In the case of

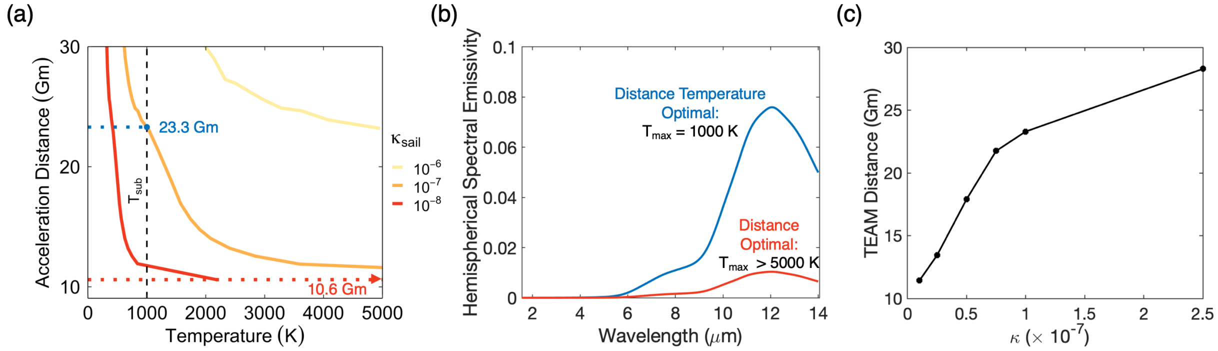

Figure 2.3: Emissive properties of multilayer photonic sail structures for a 1 g payload. (a) Minimum acceleration distance as a function of temperature for three imposed values of sail material extinction coefficient. The vertical black dotted line marks the defined ultra-high vacuum thermal limit. On the central curve ($\kappa = 10^{-7}$) the blue point and accompanying line mark the acceleration distance and temperature of the TEAM design. The TEAM design is that which obtains the TEAM distance, i.e., that which has the shortest acceleration distance among those design alternatives whose temperatures do not exceed the thermal limit. The red dotted line marks the minimum acceleration distance achievable in our design space, and demonstrates that the corresponding design has a peak temperature > 5000 K for $\kappa = 10^{-7}$, meaning the corresponding red point is not visible. The solid red curve corresponds to a simulated value of $\kappa = 10^{-8}$, which shows a solution below 5000 K, but it is still more than double the enforced thermal limit. Decreasing κ has the effect of decreasing the TEAM distance from 23.3 Gm to 11.4 Gm. (b) Comparison of the hemispherical emissivity spectra, i.e. the direction-averaged spectral emissivity, of the simple acceleration merited design corresponding to the off plot red point in (a) vs. acceleration-temperature co-merited design corresponding to blue point in (a). Calculated maximum temperatures of the designs are also provided. (c) Plot showing thermally endurable acceleration minimum (TEAM) distance for six selected values of κ, connected to show trended behavior. Values of κ greater than the plot range have no solution within our simulated sail set, meaning layers of Si_3N_4 thicker than 110nm are necessary to maintain thermal integrity of the sail in flight.

lightsails, a trade-off exists between thermoregulation and acceleration distance. In general, for a given sail diameter, increasing mass increases acceleration distance, while increasing emissive material mass enhances heat dissipation. However, greater material mass can also result in greater laser absorption. We apply these considerations by simulating our sail designs at three material extinction coefficient values of $\kappa = 10^{-8}$, 10^{-7}, and 10^{-6} for both Si_3N_4 and MoS_2 over the laser band. These coarse choices are due to the aforementioned lack of material extinction coefficient data in the Doppler-shifted laser band. We can then use the resultant absorptivity values to show the relationship between acceleration distance and operating temperature for a given κ in Figure 2.3a. These results can also be stated in terms of assumed total sail absorptivity (Supporting Information). This result clearly illustrates the effect of extinction coefficient on sail survivability. As extinction coefficient values are increased for the constituent materials, acceleration distances below a threshold value become thermally impossible to achieve. The horizontal lines are iso-acceleration distance lines, and their intersections with the curves mark extinction coefficients for which sails with a given acceleration distance value exist.

We now define a new and final composite figure of merit for our sail design space, which we call the Thermally Endurable Acceleration Minimum (TEAM) distance value. The TEAM distance value for a design space is the minimum acceleration distance among designs where $T_{sailmax} < T_{limit}$. Likewise, the TEAM sail design is the sail configuration that results in the TEAM distance value. Minimizing TEAM distance is desirable, but we emphasize that this is not a sail *metric* per se; rather, it is a summary value that can be easily reported to compare design approaches and sail datasets, rather than individual sails. Given laser parameters, payload mass, and sail architectures with known acceleration distances, TEAM distance depends on three quantities: the previously set maximum allowable sail temperature determined by the UHV sublimation limit (and therefore the high vacuum properties of the materials system used for sail design), the laser band absorption properties of the sail, and the thermal emissivity of the sail. After both high vacuum thermodynamic and high sensitivity absorption properties of candidate materials are fully determined, this can act as a simple way to compare design spaces without ambiguity.

Using our analysis framework for an imposed extinction coefficient of $\kappa = 10^{-7}$ we demonstrate a TEAM distance value of 23.3 Gm, a 12.7 Gm accelerative penalty relative to the original 10.6 Gm minimum distance, which prevents MoS_2 sublimation by limiting the sail's peak temperature to $T_{max} = 1000$ K. Addition of a 1 g mechanical backbone results in a larger TEAM value of 76.7 Gm. This design has a period of 1.08 μm, a hole diameter to period ratio of 0.1, a top Si_3N_4 emissive layer of 10 nm, a 50 nm thick high index MoS_2 layer, and a 5 nm bottom Si_3N_4 layer. Our TEAM-derived sail design has a smaller hole radius and thicker Si_3N_4 layers relative to the original 10.6 Gm design. Comparing the spectral hemispherical emissivity values of the two designs (Figure 2.3b) reveals that the thicker, larger emissive area design is necessary to radiate away excess energy and survive. The TEAM design has an approximately 8× higher peak emissivity value due to the presence of more Si_3N_4 in the photonic crystal structure. Figure 2.3c shows TEAM value as a function of κ in the laser band. When κ increases, the TEAM distance increases, placing firm bounds on allowable material absorption given a target acceleration distance.

Previously-developed photonic lightsail designs are limited to single-scale photonic features and their associated thermal characteristics. However, a multiscale segmented design architecture could yield additional thermal benefits without incurring a mass penalty. To explore this, we propose and investigate an emissivity-enhancing multiscale Mie resonant structure with thermal wavelength-scale Mie resonators patterned with laser-wavelength-scale photonic crystal features (Figure 2.4a). These multiscale photonic structures yield a large number of resonant peaks over desired peak thermal wavelengths that collectively enhance the total hemispherical emittance of the sail. This is reminiscient of nanophotonic light trapping approaches to solar absorption, where numerous peaks contribute to a large scale enhancement of absorption[67,68]; here we apply these light trapping techniques for emissive gains. Our design is composed of two 30 nm emissive Si_3N_4 layers surrounding a 90 nm MoS_2

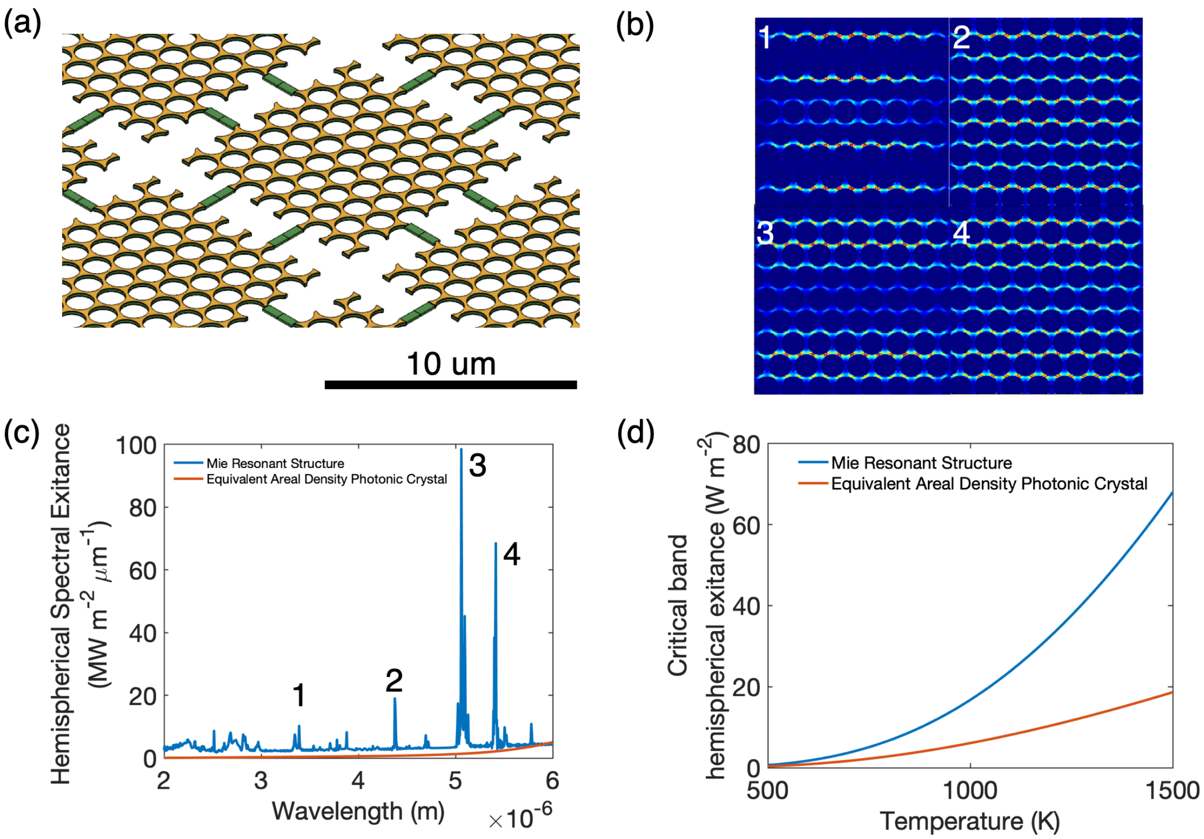

Figure 2.4: (a) Mie resonant enhancement schematic diagram illustrating the proposed multiscale Mie resonator design. The green strips show the possibility of scaffolds used to support the Mie resonator structure. (b) Spatial absorption profiles of Mie resonances in (c) corresponding to the respectively labelled spectral peaks. (c) Hemispherical exitance of Mie resonant structure vs. conventional photonic crystal structure, calculated at a temperature of 1000 K, demonstrating a pathway for possible emissivity enhancement. (d) Demonstration of spectrally integrated hemispherical exitance enhancement as a function of temperature.

core. The patterned photonic crystal has a period of 1.14 μm, with a 90% hole diameter to period ratio. The Mie structure is 8.55 μm by 8.55 μm and the overall period is 10 μm. The Mie structure achieved an acceleration distance of 16.7 Gm compared to 24 Gm for a continuous non-Mie design with similar areal density. Importantly, the Mie structure's additional emissivity in the critical 2-6 μm band lowers the sail's peak temperature. Remarkably, the Mie resonant design has a 7.4 Gm shorter acceleration distance or a 43% decrease as compared to the equivalent continuous design. Because the areal density of Si_3N_4 between the compared designs is nearly the same, longer wavelength thermal emissive features will be maintained between the two designs, meaning the additional emissivity features in the critical band from 2-6 μm are key to enabling lower overall temperatures. The structure can be connected by a series of thin scaffolds while maintaining the presence of resonant modes. If further mechanical robustness is desired, a mechanical backbone could be added.

The spatial profiles of four resonant modes supported by the multiscale Mie-resonant structure are shown in Figure 2.4b, corresponding to four modes in the 2 - 6 μm band shown in Figure 2.4c. Figure 2.4c shows the hemispherical direction-averaged spectral exitance in this band, determined by weighting the hemispherically direction averaged emissivity spectrum of the device with the spectrum of a 1000 K blackbody. This wavelength band is critical for sail heat management due to the blackbody peak position at temperatures from 500 - 1000 K, as determined by Wien's law. Increases to sail emissivity in the 2-6 μm band will more strongly reduce overall sail temperatures in comparison to emissivity increases at longer wavelengths. The enhancement of in-band hemispherical exitance at a given temperature is demonstrated in Figure 2.4d, showing that at the previously suggested thermal limit of 1000 K, the islanded design has over 2.75× greater hemispherical exitance, with as much as 3.6× the hemispherical exitance at 1500 K. This showcases the utility of the multiscale Mie-resonant structures in thermal regulation of ultralight photonic structures.

In conclusion, we have demonstrated holistically viable multilayer 2D photonic reflector designs for laser-driven lightsails that are able to accelerate to one fifth the speed of light over distances comparable to, and in some cases even exceeding, designs reported previously. We emphasize that our designs represent the entire sail structure and do not require additional backing material for emissivity enhancement, allowing for accurate modeling of payload-driven performance. To analyze such relativistic lightsail designs, we further proposed an analysis framework that accounts for both acceleration distance and peak temperature. We then proposed the thermally endurable acceleration minimum (TEAM) distance value as a summary statistic to determine the fastest-accelerating thermally-stable sail design of a design set. This value is easily reportable and will allow future engineers to compare their design sets, represented by a variety of materials, nanoscale geometries, etc. Finally, we introduced a multiscale sail design employing thermal-wavelength-scale Mie-resonant features to enhance the mid-infrared emissivity of lightsails while preserving their underlying acceleration distance characteristics. Although relativistic lightsails impose stringent constraints, our multi-scale photonic designs highlight intriguing optical capabilities that ultralight, nearly-massless photonic structures can enable over an ultrabroadband wavelength range. This in turn heralds the possibility of new classes of ultralight photonic structures that can perform as well as conventional photonic structures for mass-constrained aerospace, imaging and information processing applications.

2.7 Supporting Information

We performed simulations in S^4, an open source RCWA solver[69]. We used Si_3N_4 thermal wavelength range n and k data from Kischkat et al.[56], while we used Si_3N_4 laser Doppler-shifted wavelength n data for reflectivity from Luke et al.[70]. We used MoS_2 Doppler-shifted laser wavelength n and k data from Ermolaev et al.[48], with thermal n data assuming a value of the longest wavelength datum and k data set to 0 (a conservative assumption for thermal emission). We performed emissive (output power determining) simulations over a wavelength range of 1.55-14.05 μm. We performed reflective (input power and acceleration distance determing) simulations at normal incidence over a wavelength range of 1.2-1.6 μm. In S^4, absorption is determined (for the purpose of determining sail emissivity using Kirchoff's first law) by finding the flux through virtual surfaces on the front side (the side facing the Earth-based laser array, upon which laser light would be incident) and back side (the opposite side, facing away from earth, which laser light would be transmitted away from) of the design. Incident and reflected flux values are determined using the front surface, and transmitted values from the back surface. S^4 reports the z-component of power flux values, that is, the component of flux normal to a given surface layer. It reports these values in normalized arbitrary units. Light normally incident to a surface would therefore return an incident flux value of unity. Light incident at $\pi/6$ rad (30°) would return an incident flux value of $\cos(\pi/6) = 0.5\sqrt{3} \approx 0.87$ even though the wave still has a full incident flux of unity (the different value resulting from the component of the flux now in the transverse direction, i.e. the in-plane direction and not the plane normal direction). To correct for this, incident, reflected and transmitted values are simply divided by the incident value to normalize, then subtracted in the usual fashion. That is:

$$\alpha(\lambda,\theta,\phi) = \frac{incident(\lambda,\theta,\phi)}{incident(\lambda,\theta,\phi)} - \frac{reflected(\lambda,\theta,\phi)}{incident(\lambda,\theta,\phi)} - \frac{transmitted(\lambda,\theta,\phi)}{incident(\lambda,\theta,\phi)} \tag{2.3}$$

Data for absorbed light is taken for both s and p polarization states, then averaged as

$$\alpha(\lambda,\theta,\phi) = \frac{\alpha(\lambda,\theta,\phi)_s + \alpha(\lambda,\theta,\phi)_p}{2} \tag{2.4}$$

to obtain the polarization-averaged response, as thermally emitted light will be unpolarized.

We then assume that the sail is in quasi-thermal equilibrium while it heats due its nanoscale thickness, implying we can apply Kirchoff's first law: $\alpha(\lambda,\theta,\phi) = \epsilon(\lambda,\theta,\phi)$. While in general these two quantities depend on temperature, we decided to adopt only room-temperature values (300 K) because of the lack of temperature-dependent optical data available in the literature. Further investigation into the thermo-optic effects of candidate materials at temperatures ranging from 500 to 2000 K will be important future considerations into sail material viability.

From here, employing the equality established above, we can then take the directional average of our design in conjunction with the known black body emissivity of unity in all directions to determine the hemispherical emissivity:

$$\epsilon(\lambda) = \alpha(\lambda) = \frac{\int_0^{2\pi}\int_0^{\frac{\pi}{2}} \alpha(\lambda,\theta,\phi) * \cos\theta * \sin\theta d\theta d\phi}{\int_0^{2\pi} d\phi \int_0^{\frac{\pi}{2}} 1 * \cos\theta * \sin\theta d\theta} \tag{2.5}$$

Due to decreasing accuracy and appearance of NaN values at high glancing incidence angles, we simulated hemispherical absorbtivity of each continuous design over a polar (θ) incident angle range from 0 to $5\pi/12$ (75°) degrees in $\pi/12$ (15°) angular steps. We simulated a subset of representative values over the whole design space (all periods, all scales, and thickness values of 5, 10, 30, 50, 70, 90, and 110 nm for each layer that still capture the full range of originally simulated values) in this fashion, then linearly interpolated in MATLAB for the rest of the space. As the continuous sail design is six-fold symmetric due to its close-packed structure, it will have equivalent behavior for any azimuthal (ϕ) rotation of $\pi/3$ (60°). For this reason, we performed integration only for azimuthal angles of 0, $\pi/12$ (15°), $\pi/6$ (30°), and $\pi/4$ (45°). Substituting in these integral bounds then gives us the final equation used to determine spectral direction averaged emissivity:

$$\epsilon(\lambda) = \alpha(\lambda) = \frac{\int_0^{\frac{\pi}{4}}\int_0^{\frac{5\pi}{12}} \alpha(\lambda,\theta,\phi) * \cos\theta * \sin\theta d\theta d\phi}{\int_0^{\frac{\pi}{4}} d\phi \int_0^{\frac{5\pi}{12}} 1 * \cos\theta * \sin\theta d\theta} \tag{2.6}$$

In the case of our singular Mie structure, simulation was performed using Lumerical FDTD simulations, as S^4 does not handle the multi-scale structure we present elegantly. In this case, simulation was performed for both polarizations in $\pi/6$ (30°) polar steps from 0 to $\pi/3$ (60°) and $\pi/6$ (30°) azimuth steps from 0 to $\pi/2$ (90°) over the 2-6 μm range shown.

Once spectral emissivity is known, temperature can be calculated using equation (2) in the main text, repeated below:

$$P_{sail}\alpha_{sail} = 2A_{sail}\int_a^b \frac{c_1}{\lambda^5} \cdot \frac{\epsilon_{sail}(\lambda)}{e^{\frac{c_2}{\lambda T_{max}}} - 1} d\lambda \tag{2}$$

The left side represents the power absorbed by the sail, and the right side is simply the spectral emissivity multiplied by Planck's law at a given temperature. The temperature is raised from 0 K, the equality is checked, and when the difference between these two quantities is less than 100 W (This tolarance $10^{-7}\%$ of the incident power on the sail and 1% of the absorbed power), the temperature is recorded for the corresponding design. This is the reported maximum steady-state temperature used in our analysis.

2.7.1 Thermal Limit

The conservative upper temperature limit applied to MoS_2 is based on the ultra-high vacuum (UHV) melting temperature of MoS_2, which had the lower value of the two materials in our sail. Based on previous thermodynamic analysis, the decomposition of MoS_2 to Mo_2S_3 occurs at ~1250 K for a pressure of 10^{-4} Pascals[59,60]. Ultra-high vacuum is conventionally defined to begin at pressures of 10^{-7} and below. Extrapolating from the known data, we set a max temperature of 1000 K for UHV pressures, but later precise experimental measurements at these pressures could alter this value.

2.7.2 Payload Mass Effect

For our design space, the design with the lowest acceleration distance given by (1) in the main text increases linearly as a function of payload mass. This is to say, we find that the best sail-payload system possible for a given payload mass has a lower limit tied to the overall mass of the system, shown in S1. The slope of this line is 4.31 Gm/g, meaning that each gram of payload mass added to our system will increase the acceleration distance by approximately 4 Gm.

2.7.3 Form of $h(\beta)$ and influence on design

The plot the $h(\beta)$ function over the relevant range of β values is shown in S2. This can essentially be thought of as a weighting function of $\frac{1}{R(\beta)}$. Given a constant irradiance on the sail this means that high reflectivity is more desirable at higher doppler shifted wavelengths. We note that this is not necessarily true if irradiance on the sail changes as the sail accelerates.

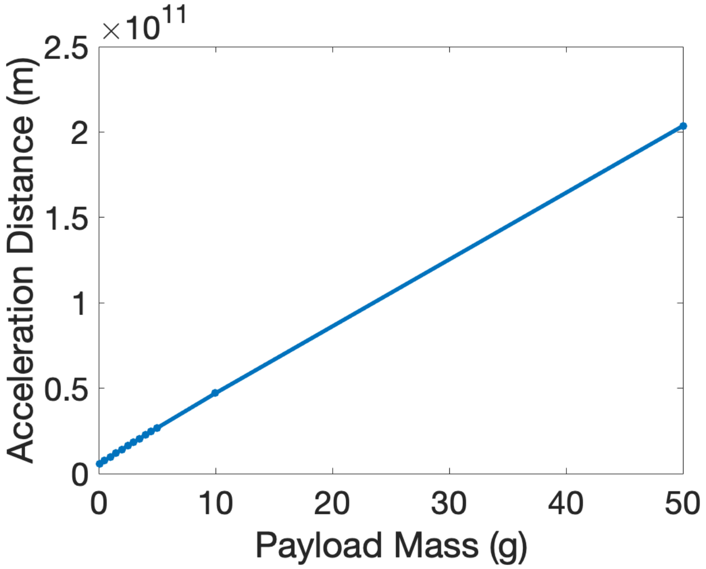

Figure 2.5: Demonstration of correlation between payload mass and acceleration distance. Each gram of mass adds approximately 4 Gm of acceleration distance to the system.

2.7.4 Alternative form of acceleration vs. temperature plot

For comparison to other groups who show assumed absorptivity of the sail as opposed to extinction coefficient, S3 shows an alternative form of figure 3a that is more comparable. We note that this is not a materially generated value of absorptivity, but an assumed value of absorptivity for the entire sail stack.

2.7.5 Form of the Power Balance Equation

Physical and optical property material data do not exist for every material over every wavelength range. Because of this, evaluating the total radiant exitance of a real material is not generally possible. With this consideration in mind, it is more practical to use definite integral bounds for known material data. The solution in terms of T_{max} to equation (2) from the main text, reiterated below:

$$P_{sail}\alpha_{sail} = 2A_{sail}\int_a^b \frac{c_1}{\lambda^5}\cdot\frac{\epsilon_{sail}(\lambda)}{e^{\frac{c_2}{\lambda T_{max}}}-1}d\lambda \tag{2}$$

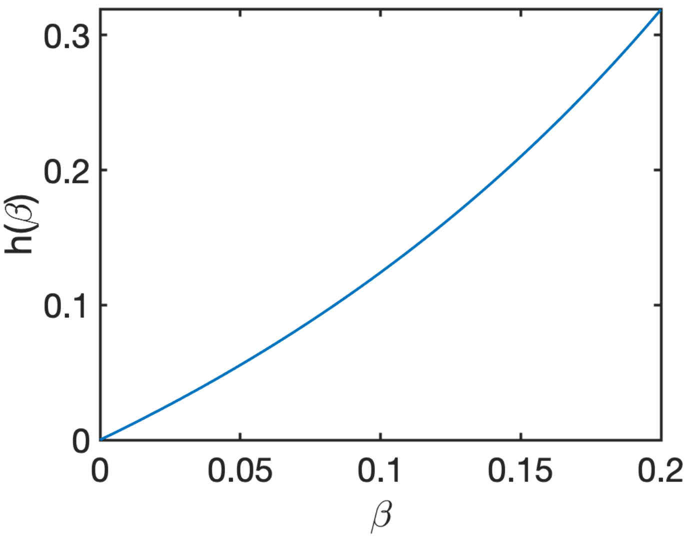

Figure 2.6: Simple plot of $h\beta$ function showing its monotonic increasing behavior, demonstrating that reflectivity at higher velocities is weighted more heavily then reflectivity at lower velocities

α can then be found as

$$\alpha_{sail} = \frac{1}{\lambda_f - \lambda_0} \cdot \int_{\lambda_0}^{\lambda_f} \alpha(\lambda) d\lambda \tag{S5}$$

where λ_0 and λ_f are the initial and final Doppler-shifted laser wavelengths respectively. In this case they would correspond to values of 1.2 μm and 1.47 μm. When a and b are both finite bounds, S5 does have an analytical solution for a blackbody (the case where $\epsilon(\lambda) = 1$) but even this is quite cumbersome[71]. In the event that ϵ varies with wavelength, as in a real material, analytical integration is not generally used. As such numerical integration is preferable and by determining our maximum temperature through numerical integration, current material data can easily be used, and simply added to other data ranges of known data.

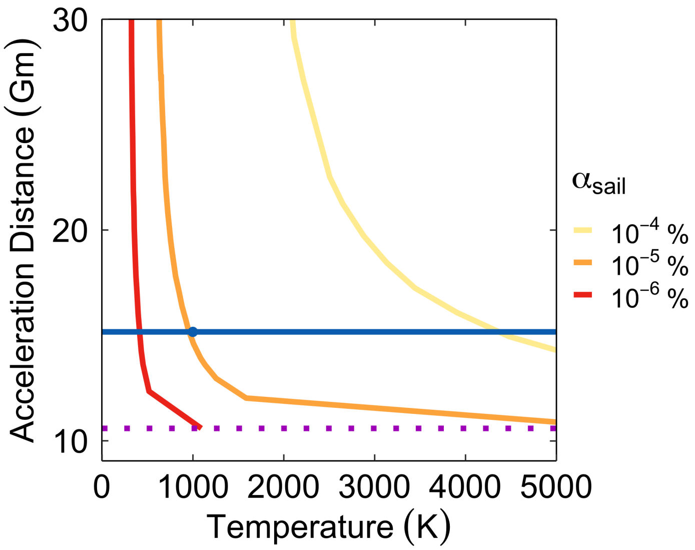

Figure 2.7: Plot of $h\beta$ function showing its monotonic increasing behavior, demonstrating that reflectivity at higher velocities is weighted more heavily then reflectivity at lower velocities

2.7.6 Acceleration Distance Comparison of Mie Structure Vs. Continuous Structure

This section confirms the accelerative performance of our Mie resonant structure based on reflectance and weight based considerations. In our manuscript, we compare two structures that have similar areal densities per layer. The first is a continuous structure consisting of an 8.43×10^{-14} g/um^2 reflective MoS_2 layer surrounded on both sides by emissive Si_3N_4 layers of areal density 1.91×10^{-14} g/um^2. The second is the islanded structure described in the manuscript, with a reflective MoS_2 layer areal density of 8.58×10^{-14} g/um^2 and surrounded by emissive Si_3N_4 layers with areal densities 1.9445×10^{-14} g/um^2.

2.7.7 Connected Mie Resonant Structure

The Mie structure as given in our work, shown in Figure 4a, is a design to be connected via thin MoS_2 scaffolds. Based on simulations performed, the emissive merit of this design is high, but its reflective merit is somewhat low. For a more structurally-robust design that maintains reflective merit at a cost of some emissive merit, the central MoS_2 layer can be made continuous, while the Si_3N_4 layers atop and below it remain islanded, as in the initial design. A concept drawing of this design is shown in Figure S3. This design preserves the structure of the more familiar photonic crystal reflector, while adding Mie resonant islanded structures that have decreased emissive benefit compared to the fully islanded case. Overall it results in superior accelerative performance against the fully islanded design at a cost of emissivity, as it displays fewer emissive peaks in the critical 2-6 um range.

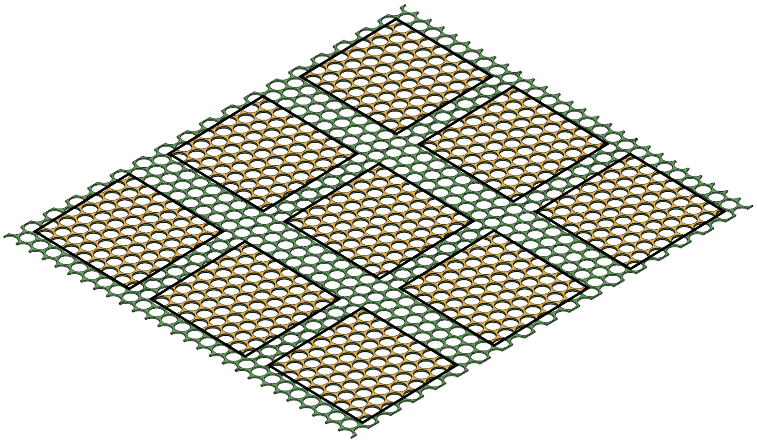

Figure 2.8: Continuous Mie structure design. The black outlines serve to highlight the positions of the Mie resonant features against the continuous reflective green layer, but would not exist in the actual design.

2.8 Opto-Mechanical Modeling assistance

The final portion of my involvement in the Starshot project was with our collaborators at UPenn[20], which I aided by sanity checking the models they were using for mechanical simulation. Because of the strong relation between the optical properties of the sail and the mechanical behavior, I helped set reasonable models for the simplified systems used for the mechanical modelling. This allowed our collaborators to set reasonable material behavior, and using our simulated values of acceleration they were able to generate stress plots to determine failure criterion of the sail. These criterion were related to maximum viable accelerations, as well as the conclusion that on the macro scale, the sail should be curved in order to limit the mechanical failure modes as the sail accelerates.

CHAPTER 3

Resonant Anti-Reflection Metasurfaces for Infrared Transmission Optics

fundamental capability needed for any transmissive optical component is anti-reflection, yet this capability can be challenging to achieve in a cost-effective manner over longer infrared wavelengths. We demonstrate that Mie-resonant photonic structures can enable high transmission through a high-index optical component, allowing it to function effectively over long-wave infrared wavelengths. Using Silicon as a model system, we demonstrate a resonant metasurface that enables a window optic with up to 40% greater transmission than unpatterned Si. Imaging comparisons with unpatterned Si and off-the-shelf Germanium optics are shown, as well as modulation transfer function measurements, showing excellent performance and suitability for imaging applications. Our results show how resonant photonic structures can be used to improve optical transmission through high-index optical components, and highlight their possible use in infrared imaging applications.

3.1 Background

Increasing the transmission efficiency of optical components is broadly desirable in optical system design across all wavelengths. In the long-wave infrared band from 7 to 14 μm, for applications such as thermal imaging, high transmission efficiency is key for desirable performance due to the intensity-sensing nature of microbolometer-array-based detectors[72,73]. Single-layer or multilayer thin film interference coatings are today's standard for anti-reflection and transmission enhancement and are well developed[74–76]. However, this approach requires materials specific coating stack engineering, which can be difficult and time-consuming depending on the system[77–82]. This is because coating materials with a desirable refractive index and absorption over a given band may not exist and must be mechanically compatible with other stack materials. These difficulties are compounded by the desire for stacks that achieve some combination of durability, angular acceptance, and polarization insensitivity. Over longer wavelengths, thicknesses of the layers and the overall stack increase substantially, resulting in both added costs and limits to performance.

An alternative approach to anti-reflection is to use gradient index structures. To enable a gradual change in the refractive index along a depth dimension, gradient index structures typically employ depth modulated material-aggregate/sol–gel-based coatings or, alternatively, use so-called "moth-eye" anti-reflective structures. In the aggregate approach, nanoparticles are aggregated or created using processed chemical precursors, with sol–gels generally used to tailor particle densities at the interface in order to achieve a gradient index[83–87]. Other recent methods have used spinodal separation methods followed by etching to create porous structures[88,89]. In contrast, moth-eye geometries take advantage of subwavelength porous or high aspect ratio cone and pillar geometries which are fabricated by directly etching the surface of a substrate, and which can be treated as effective media used to minimize index mismatch between air and the higher-index substrate[90–97]. While these approaches can compete with and exceed thin-film-coating-based approaches in terms of raw transmission, there is evidence that random structures can exhibit significant diffuse scattering depending on their geometry[98,99], which would cause reduced contrast when used for imaging. Additionally, the geometries of these structures often result in increased mechanical fragility and susceptibility to environmental contamination and abrasion, which can greatly reduce their performance over time in harsh environments[100–103].

More recently, another approach to anti-reflection has emerged that uses resonant photonic structures at the interface between two media to decrease reflection. Unlike gradient-index-based approaches, resonant anti-reflection approaches use subwavelength photonic structures that are mechanically durable, robust, and easily fabricable. Early work investigated using metallic surface resonator elements which leveraged dipole resonances to achieve anti-reflection and preferentially forward scatter light[104–106]. Later work introduced an alternative method employing all-dielectric Mie-resonant structures[107–111]. This approach has primarily been explored over visible and UV wavelengths for absorption enhancement in solar cell applications. Early work from Spinelli et al. showed that monolithically coupled nanopillar structures exhibited scattering cross-sections up to 5 times larger than their geometrical cross-sections. This, in conjunction with the overlap of the resonant modes in the nanopillars with propagating modes of the substrate, results in a leaky mode that preferentially forward scatters into a high index material. The specific overlap of magnetic and electric dipole modes determines the resonance shape and is what allows the ensemble response to reproduce the incident wave into the substrate. The anti-reflection effect is enabled as a result of destructive interference between these electric and magnetic dipole modes[112], also referred to as the substrate-mediated Kerker effect[113]. Theoretical conditions to maximize the effectiveness of this resonance-based approach have been established[114]. Further developments enhanced the bandwidth of anti-reflection using multiresonant structures[115], as well as the previously discovered effective index support[116] of Fabry–Perot resonances[117].

While actively explored for solar absorption enhancement, to our knowledge, resonant anti-reflective approaches have not been demonstrated for transmission optics. Anti-reflection for imaging must enable high throughput and preservation of the incident wavefront through both high index interfaces. This capability, if possible to enable by the Mie-resonant approach, is of particular interest in long-wave infrared optical components, where anti-reflection via either conventional thin film or gradient index approaches can be challenging while meeting environmental and imaging-based constraints.

Motivated by these considerations, we propose and experimentally demonstrate a resonant anti-reflection approach to maximize transmission through an optical component while maintaining overall image quality. We design and optimize Mie-resonant nanophotonic structures and show through simulations that the overall phase front of incident light is preserved, meeting the key capability outlined above. We then fabricate the nanophotonic structures at the wafer scale on both sides of a double side polished (DSP) Silicon wafer, demonstrating strong anti-reflection and transmission over the LWIR wavelength band, with up to 40% transmission enhancement relative to unpatterned Si. We furthermore measure and calculate a modulation transfer function (MTF) of the Mie-resonant-structure-treated Si wafer and demonstrate image quality preservation, enabling utilization of this approach even for high-resolution imaging applications. Importantly, our approach shows equal or better transmittance than the previously mentioned coatings on Si at all investigated angles in the thermal band. Further, its transmittance performance is comparable to off-the-shelf broadband anti-reflection coated germanium alternatives at peak transmittance wavelength, enabling an alternative lower-cost material for window optics in LWIR and thermal imaging applications.

3.2 Design: Materials and Simulation

While Mie-resonant anti-reflection has been actively explored for absorption enhancement, there are important considerations that differentiate its utilization for imaging through transmission enhancement. Broadly, we group the goals of anti-reflection into three main categories, depicted in Figure 1. The first category is absorption enhancement, motivated by applications such as solar cells. Here, the back plane of the cell is typically assumed to be diffuse and fully reflective, and no light transmits through. Light is intended to be coupled into the media and absorbed as efficiently as possible to generate the greatest photocurrent. The second category corresponds to a transmissive back plane (such as in multijunction cells) which only considers maximization of optical power of a given band with no regard to image preservation. The final category considers the scenario in which power throughput is maximized while also ensuring image preservation. The concept of “image preservation” is meant to convey that the wavefront integrity is preserved and not degraded to a degree which makes resolving an object impossible. Our investigation focuses on this final case, which has not been explored in the LWIR range using a resonant-based approach to the best of our knowledge.

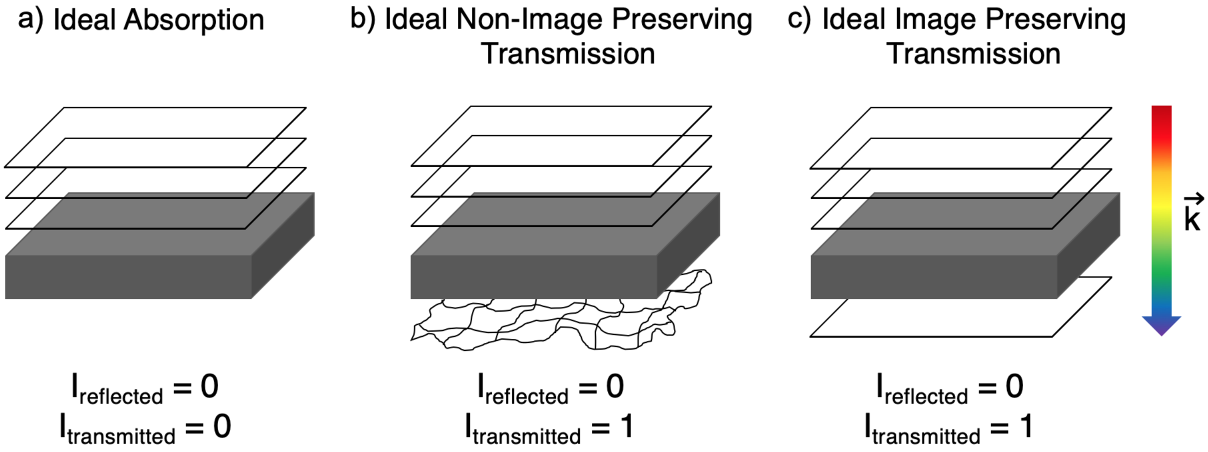
a) Ideal Absorption
b) Ideal Non-Image Preserving Transmission
c) Ideal Image Preserving Transmission
$\vec{k}$
$I_{reflected} = 0$
$I_{transmitted} = 0$
$I_{reflected} = 0$
$I_{transmitted} = 1$
$I_{reflected} = 0$
$I_{transmitted} = 1$

Figure 3.1: A schematic comparison of anti-reflection for a) Absorption enhancement: In this case, waves enter the substrate but do not leave it, being absorbed either as heat or generating photocurrent. As they are not exiting, their output state is disregarded. b) Non-image preserving transmission enhancement: In this case, waves enter the substrate and are scattered by either or both of the front and rear surfaces. This configuration could occur in a multijunction cell, or any diffuser optic. c) Image preserving transmission enhancement. In this case, the shape of the incoming wave is preserved as it exits the substrate optic. Input plane waves exit as plane waves, and waves with more complex wave fronts will be maintained with an added phase due to propagation.

Dielectric Mie resonators can induce excellent anti-reflection through the unique forward scattering phenomena enabled by an ensemble response of individual resonators. In our case, a subwavelength periodic array of resonators causes enhanced transmission through the interfaces of Si at the relevant LWIR wavelengths which maintains the integrity of the overall input wavefront. This approach is in principle highly broadband and omnidirectional and has minimal polarization sensitivity, all of which are desirable properties for an imaging optic. Additionally, the approach is entirely binary, enabling fabrication by conventional photolithographic means. We note that going against conventional Fresnel-law-based intuition, the all-dielectric Mie-resonant approach relies on a large index contrast in order to produce high quality suppression of reflections. Optical materials generally used for transmission optics in the LWIR wavelengths, such as Ge and, as we will demonstrate, Si, have suitably high refractive indices. This presents a unique opportunity to use the resonant approach to increase transmission efficiency in these wavelengths despite the large index contrast normally resulting in a poorer reflective performance.

We opted to use Si as our material system due its wide availability, fabrication maturity, and relatively low overall transmittance in the LWIR[118,119] (~50% through a 500 μm thick bare substrate over the full $\lambda = 7-14\ \mu m$ band) which allows for significant and easily noticeable performance improvement. We applied the resonant approach to arguably the simplest optical component, a window. Window optics provide a clear and useful proof-of-concept platform for our approach. They are ubiquitous for protection of sensitive components in optical systems from the environment and often necessary to prevent ingress of dust and humidity to the rest of a lens column. As noted above, Si's relatively high intrinsic absorptivity in the LWIR means that it is not typically used for imaging or window optics in the face of higher transmission Ge, ZnSe, or ZnS alternatives. We note however, that large thicknesses may not be essential in fulfilling a window's protective functionality (i.e., when impact resistance or high pressure tolerance is not a necessary function of the window). In cases where imaging is desirable, more recent advances in metasurface design demonstrate that thin and flat focusing optical systems are possible, limiting the effects of Si's intrinsic absorptivity on optical performance. Additionally, Si does hold notable mechanical advantages over the previously mentioned materials, having a lower density and higher hardness[120–124]. Finally, there is evidence to suggest that in high temperature ambient environments, the absorptivity of Ge may exceed Si at thermal wavelengths[125,126], making Si an even more viable alternative in high temperature operation.

We first numerically investigated and optimized resonant anti-reflective designs scaled for Si's index and the LWIR wavelength range, evaluating a range of different lattice and feature geometries assuming 2 identically patterned interfaces. We simulated the designs using rigorous coupled-wave analysis (RCWA) while assuming fabricable critical feature sizes based on available tooling. To facilitate optimization, we developed a custom figure of merit shown as eq 1 which rewarded integrated spectral transmittance through the optic while inflicting a severe penalty on unfabricable designs:

$$FOM = \begin{cases} \int_{7\mu m}^{14\mu m} T(\lambda) d\lambda + \int_{7\mu m}^{9\mu m} T(\lambda) d\lambda, & \text{if } d_{critical} \geq 0.5\ \mu m \\ 0, & \text{otherwise} \end{cases} \tag{3.1}$$

The result of this optimization, shown schematically in Figure 2a, yielded the best performance of the designs explored within typical wafer-scale fabrication limits. We note here that the added 7–9 μm integral term sought to reward higher transmission at more energetic wavelengths, but in principle, resonator geometries could be tailored to move the peak to longer wavelengths as well. E-field component plots for a demonstrative 16 μm thick Si substrate are shown in Figure 2b, which show the aspect of our design that is of particular importance to our application: the coherent character of the forward scattered waves through the interface, resulting from the overlap of electric and magnetic dipole resonance overlaps present. Further field plots to demonstrate the resonance shape and dipole overlap can be found in the Supporting Information. This phenomenon occurs when the waves are scattered into and out of the patterned high index media. Simulated spectral transmission comparisons are shown in Figure 2c, highlighting the transmission performance increase we expected from our approach.

We highlight a portion of the optimization landscape in Figure 2d, which shows a slice of the 3D optimization (feature height, period, and feature width) at a feature height of 1.2 μm. The y axis shows the trench width between each resonant element (the critical feature in terms of fabrication), while the x axis shows the multiplier of the trench width to determine the period. The period for a tile is then given by multiplying the x and y axis values for that tile. This allows scanning a large number of features while ensuring the prevention of unphysical or unfabricable designs.

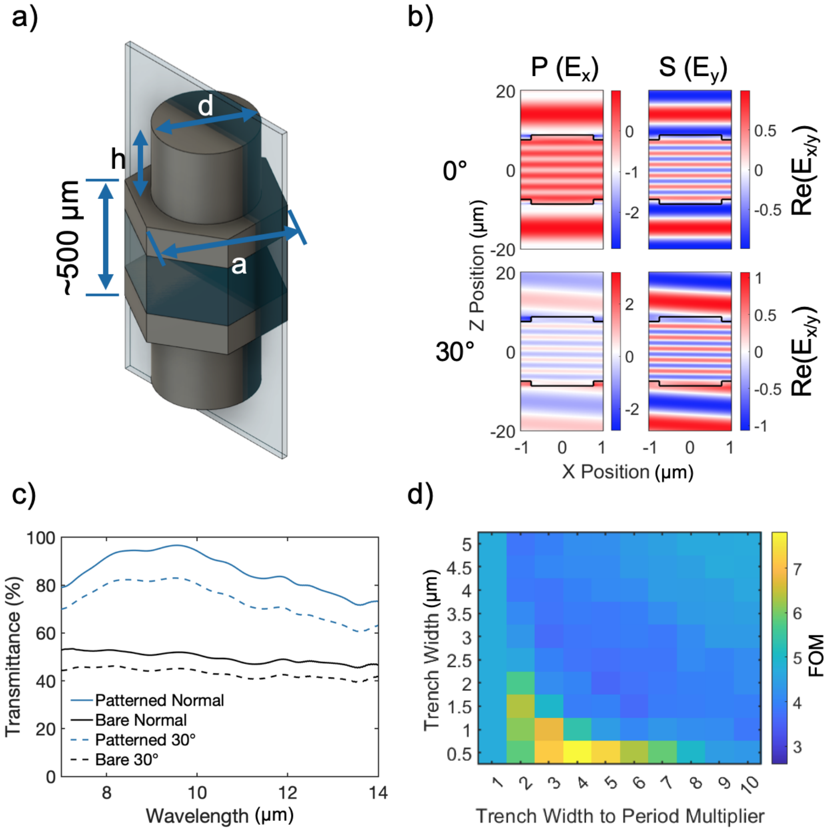

Figure 3.2: a) Pictorial schematic of a single hexagonal unit cell of finalized design. Design is patterned on both sides of wafer. $d = 1.5\ \mu m$, $h = 1.2\ \mu m$, $a = 2.0\ \mu m$, resulting in a critical trench feature size of 0.5 μm. Plane cross section through unit cell depicted in b is shown. b) E-field component plots for normal and 30° incidence. Simulation cross-section at 9.6μm for a truncated 16μm thick substrate to demonstrate plane-wave propagation, shown for P and S polarizations. c) Comparison of simulated spectral transmission for unpolarized light at normal and 30° incidence. At least a 20% uplift over the entire band and 0°-30° angular range. d) Slice of simulation parameter sweep for optimal 1.2μm cylindrical pillar feature height, showing trench width vs. period multiplier. Period for a given tile is calculated by multiplying x and y positions for that tile. Feature width can then be calculated by subtracting the y value from the resulting period.

3.3 Transmission and Imaging Characteristics

We fabricated the optimal design on float zone process grown 500 μm thick double side polished intrinsic Si substrates. We lithographically patterned the optimized Mie-resonant photonic structures of hexagonally packed cylindrical pillars with a periodicity of 2 μm, a height of 1.2 μm, and a diameter of 1.5 μm onto both sides of the wafers (see the Supporting Information). A high magnification SEM image of the design tilted at 35° is shown in Figure 3a showing good consistency and overall design fidelity.

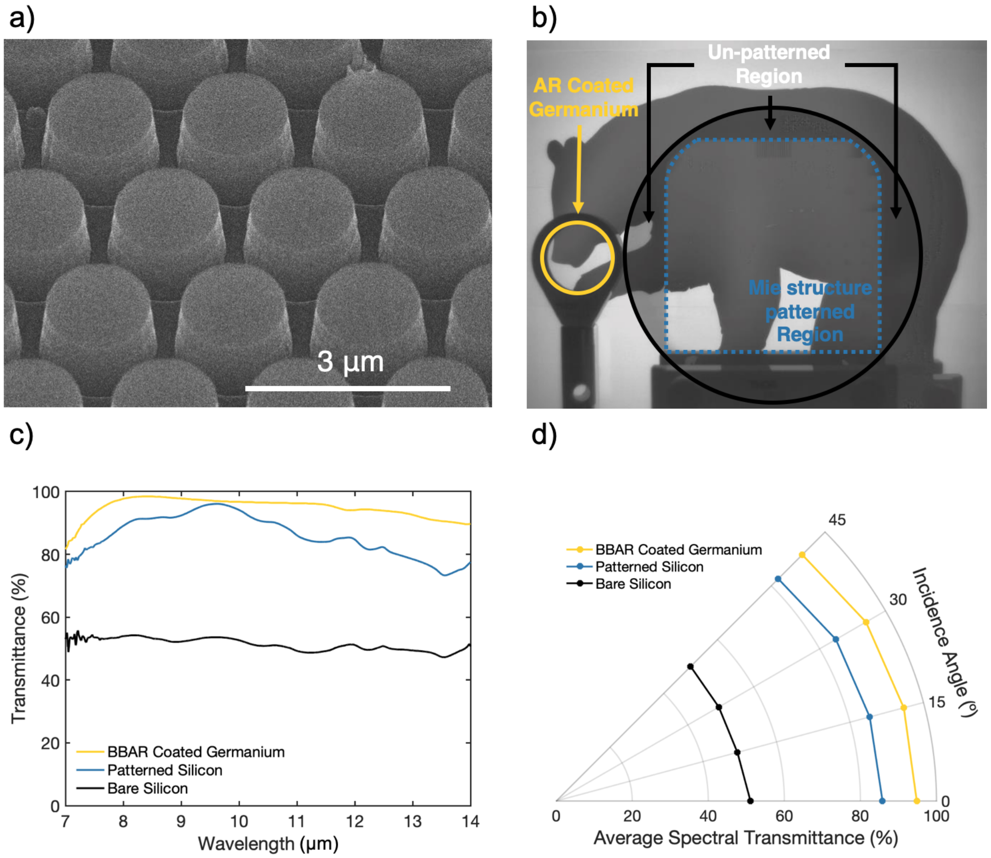

Figure 3.3: a) SEM image of surface patterning, which is present on both sides of substrate. b) Imaging test of fabricated optic taken on FLIR BOSON+ thermal camera. Borders to patterned region and wafer edge have been added for clarity, Si transmission improvement is immediately noticeable compared to unpatterned edges of wafer, and compares favorably with the Ge window on the left. c) Comparison of unpatterned (black) and patterned (blue) intrinsic Si, and AR coated Ge (yellow) windows at 0° incidence. Patterning results in an up to 40% increase in transmission over the bare case. d)Angular falloff plot showing integrated spectral transmission over the 7-14μm band for bare Si, BBAR coated Ge window, and Mie patterned Si.

LWIR spectral measurements of the device can be seen in Figure 3b, comparing the performance of a bare Si wafer, a patterned Si wafer, and a 1 mm thick Ge optic. As the design is highly periodic, diffraction is a possible concern in terms of imaging, but we note that the patterned features are small enough with respect to the 7–14 μm band that they fall outside the diffractive regime for all incidence angles ($\frac{\lambda}{a} > 2$ for the entire band). This lack of diffractive behavior is observable in the E-field component plots at each polarization for 2 cross-sectional cuts of the unit cell in Figure 2b, showing planar propagation of the waves in either polarization and at angular incidence. Finally, as the window optic will be used in an imaging system, its transmission spectra are only a proxy for its true performance. In reality, if the surface relief structure causes undesirable scattering-based effects, these will manifest only when imaging through the device. As an initial test, an image of a thermal target was taken through the patterned device, as shown in Figure 3c. The square patterned area has a dotted outline, with wafer segments outside of this area being unpatterned. A Ge LWIR AR coated window is also shown as a comparison, with areas outside both window regions acting as a control. A clear difference in transmission can be seen between these areas, while imaging integrity is maintained.

As a final, more quantitative demonstration of imaging performance, we performed a tangential broadband modulation transfer function (MTF) measurement using a slanted edge target through our patterned Si optic, an AR coated Ge window, and no window. Images were then taken at 0° (on-axis), 10° (70% field), and 14° (full-field) field angles. While the full field of view is around 15°, enough of each side of the slant target needed to be visible in the image for proper measurement. Analysis and MTF calculation was done using sfrmat5, a publically available code used for MTF measurement of systems using slant edge targets[127]. Comparisons at each field angle are shown in Figure 4, showing that the MTF is comparable between our photonic Si optic, the commercial Ge optic, and the case without a window at all 3 field angles. We note that, while this measurement was performed in as controlled a manner as possible with available equipment, it is primarily meant to demonstrate the comparison of our optic to notable alternatives and is not intended to serve as a specification for any of the individual optics or complete system under test. MTF is highly dependent on both the imaging system and the detector used, and acceptable values of MTF are highly application- and context-dependent. In our case, we have used the same detector and focusing lens column in all measurements, with the only changes being the addition of the different window optics in order to produce a useful comparison between these window components specifically and not all possible optical systems. Additionally, while the response for each case is close, Figure 4b's inset shows that the MTF with window optics added is in general higher than without. We attribute this to the frequency filtering of the windows, preferentially rejecting poorly corrected source wavelengths from entering the rest of the imaging system. These relative positions hold at 97% of the plotted points. Differences at each measured spatial frequency point for all three field angles can be found in the Supporting Information. The maximum effect with the added window over all plotted frequency points and angles only amounts to a difference of 3.6% in the modulation factor.

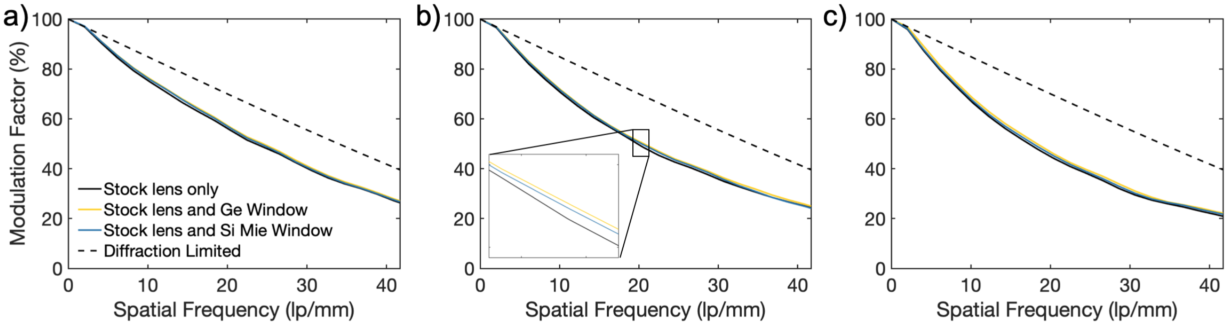

Figure 3.4: Modulation transfer function (MTF) comparison between control LWIR optical system, Ge window optic, and Mie-resonant high transmission Si a) On-axis, b) at 10° or 70% field, and c) at 14° or 93% horizontal field. MTF values are comparable between all 3 systems at all field angles, indicating that scattering from surface does not cause significant imaging performance loss. To highlight the relative magnitudes of the curves more clearly, a zoomed inset has been included in 4b, reflecting that the MTF presents as higher with additional optics, which we note is likely an artifact resulting from spectral filtering occurring from the added optics. Camera used was FLIR BOSON+, 640 x 512 pixel camera with 12 μm pixel pitch. Spatial frequency data was plotted out to detector Nyquist frequency of $41.\bar{6}$ lp/mm.

The Mie-resonance-based approach we have demonstrated here offers several possible advantages over current state-of-the-art thin film coatings at these wavelengths. While the literature investigating AR coatings for Si over LWIR wavelengths is scarce, known thin film approaches use ZnS[128] or a combination of ZnS and YF_3 as the coating material, with an Al_2O_3[129] or MgO[130] adhesion layer, respectively. While thin film adhesion and film stress are generally sensitive to growth conditions in most materials systems, highly optimized many-layer coatings with these materials have suffered from delamination issues which have not been solved[130]. These film thicknesses were generally on the order of 1–2 μm. Additionally, thermal cycling has the ability to aggravate these issues in more complex systems[131]. With these considerations in mind, although lithographic fabrication of Mie-resonant structures involves more complex processing, our AR approach holds promise for a variety of applications where thermal cycling durability, adhesion, scratch resistance, or high temperature performance are desirable. Moreover, several optics can be produced from a single wafer, and it is simple to engineer our solution and tailor its peak wavelength over the thermal band, for which a given substrate material is transparent. Compared to graded-index approaches, a Mie-resonant approach generally has similar fabrication difficulty and is less susceptible to dust, humidity, abrasion, and mechanical wear affecting its performance due to its lower aspect ratio. A cost comparison of these approaches is hard to estimate as materials prices, tool time, and inputs can vary greatly, but purely from the standpoint of substrate materials, even float zone Si is significantly less expensive than equivalent Ge substrates (see the Supporting Information).

In conclusion, we have demonstrated a method based on resonant forward-scattering microstructures to increase transmission in Si optical components over LWIR wavelengths. We show a performance increase of up to 40% with comparable performance to Ge at shorter wavelengths, where the optical power incident on the detector is greatest. We note that our approach shows equal or better performance than previously reported thin film coatings for Si at all shown angles. An intriguing future possibility exists in combining our resonant metasurface approach with focusing metasurface patterns on the opposing side of the same substrate to allow the use of Si LWIR optics, making it a viable alternative material platform in systems where throughput requirements are not as stringent. Additionally, the use of the Si in this configuration suggests intriguing possibilities for its use in active optoelectronic systems over long-wave infrared wavelengths.

3.4 Supporting Information

3.4.1 Materials and Methods

Initial fabrication was performed on 4" double side polished 500μm thick N-type silicon, which we found to be completely opaque in the infrared range using FTIR transmission measurements. These initial wafers were used to determine process flow and gain insight into how fabrication should best proceed, as well as to determine correct etch times for desired feature depth, and determine resist and anti-reflection curing and exposure properties. Fabrication proceeded onto P-type wafers, which were significantly less absorptive than purchased n-type stock and allowed determination of how fabricated devices differed from simulated geometries in spectral response. Final device fabrication was then performed on 4" double side polished 500μm thick intrinsic float zone silicon. Wafers were thoroughly cleaned out of pack in 30 minute 100°C Piranha etch bath, then spin rinse dried. After cleaning, approximately 4000 Å of wet thermal oxide was grown on wafers for use as an oxide hard mask. The first side of the oxidized wafers were then processed on an SVG 8800 track coater. On track coater, wafers were HMDS vapor primed, then spin coated with AZ BARLI ii back side anti-reflection coating at 3 krpm, followed by a soft bake at 200°C for 60 seconds. Wafers were then put back through track coater and coated with AZ MIR 701 positive tone photoresist at 5 krpm, followed by an automatic edge bead removal step. Wafers were then soft baked again at 90°C for 90 seconds.

After photoresist was applied, exposure was done on an ASML PAS 5500/200 projection exposure stepper alignment tool. Mask pattern was designed such that field could be tiled continuously across wafers with multiple adjacent exposures, though per-field alignment was not perfect, and adjacent fields generally had small misalignments. Exposed wafers were then post exposure baked at 90°C for 90 seconds. After post exposure bake, wafers were beaker developed in AZ 300 MIF developer for 60 seconds, then placed into a cascade bubbler rinse for 1 minute. Rinse was followed by a nitrogen gun dry, then hard bake at 118°C for

60 seconds.

After hard bake, wafers were then RIE fluorine etched for hard mask release. Wafers were then cleaned in a Matrix 105 oxygen plasma asher. Following plasma clean, residual photoresist was then cleaned off using 3:1 Piranha etch for 30 minutes. Wafer was then chlorine etched to desired depth in a PlasmaTherm SLR 770 ICP RIE tool.

Single side etched wafers were then taken through the above process again for the back side. After back side chlorine etch was completed, oxide hard mask present on both sides was etched away in HF dip, followed by a cascade bubbler rinse and nitrogen gun dry to complete the device. Metrology on initial fabrication attempts was done on a combination of Dektak contact profilometry and SEM image analysis to understand and characterize resist mask, hard mask, and etch depth steps. After device was completed, its spectra was measured using a Bruker INVENIO R FTIR tool to determine its IR transmission properties. IR image capture setup is described in the following section in detail.

Off-the-self Germanium window optic was a 1 mm thick 1” BBAR coated and purchased from Edmund Optics.

3.4.2 Supplemental Field Plots

Vector field plots of all E and H field components real parts at normal incidence are shown in Figure 3.5. Transverse cross-sections are taken at half the height of resonator feature, approximately 0.6 μm below top of micro-cylinder. Dipole resonance overlap is visible in the rightmost column of Figure 3.5, demonstrating the implicated phenomena which causes Mie-resonant AR behavior.

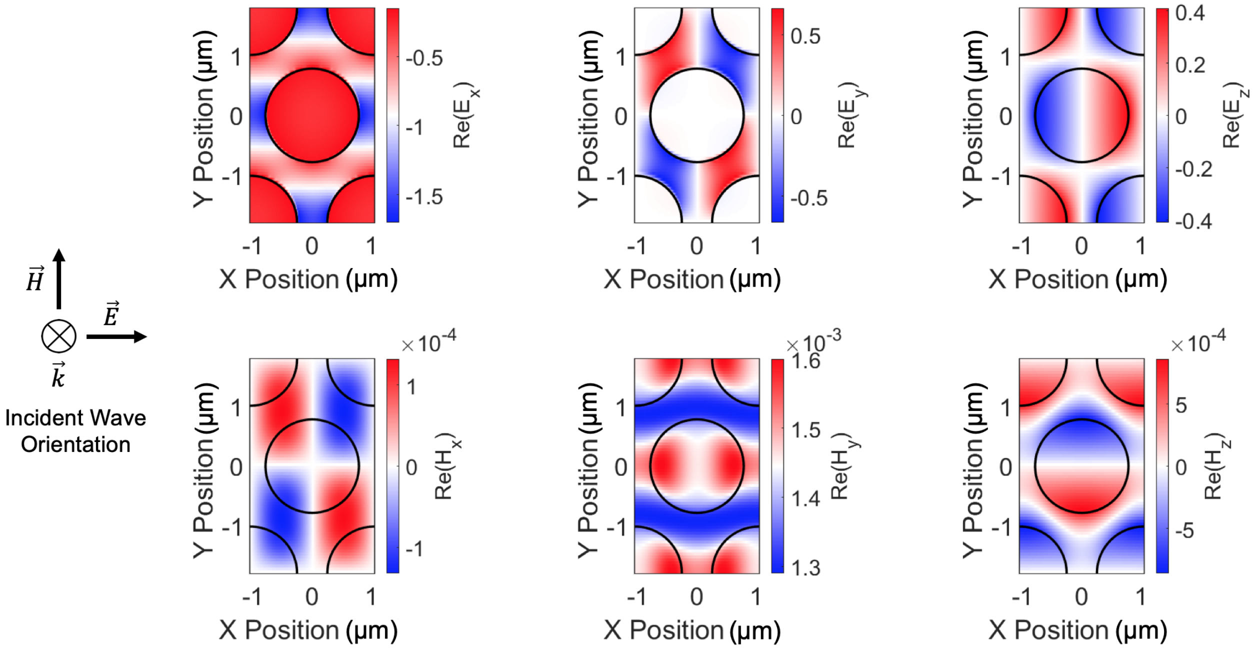

Figure 3.5: Tranverse plane field plots of Mie-Resonant AR structure at normal incidence, with structure boundaries indicated by black circles. E_z and H_z dipole resonances overlaps are visible in the rightmost column. Note that each plot has been range normalized to show greatest contrast.

3.4.3 Experimental setup of MTF Measurement

Image testing was done with FLIR BOSON+ thermal imager with 640 x 512 imaging resolution. Pixel elements have $12\mu m$ pixel pitch. Cardboard enclosure was used to block stray heat and light from lab environment from reaching detector body, and cardboard slats were used to prevent stray reflection of source light from optical table surface. Camera unit was placed approximately 2' from slant edge object which consisted of a piece of aluminum sheet metal stock placed in front of a vertically oriented hot plate surface, with an approximately 5.5° tilt applied along the factory cut edge. Aluminum object was slightly tilted with respect to normal camera incidence to prevent camera thermal signature (reflection) from affecting data collection. Hot plate was set to $100°C$ and allowed to thermally stabilize for 10 minutes before beginning image capture. High absorptivity aluminum tape was adhered to surface of hot plate to slightly flatten image field and give more greybody like response and increase target contrast. Camera was set to capture raw 16 bit .TIFF format images without software gain applied, and automatic flat field correction was turned off for image capture. For each field and device, the field was first manually flattened using software command, then a series of 10 images was taken. Images were cropped to the identical pixel locations, then cropped image counts were averaged and rounded to nearest integer count value. This final averaged image was then used to calculate MTF data. To determine imager "dark" count, a 2" x 2" piece of dry ice was imaged $< 1\ cm$ from imager lens body. This dark count value was then subtracted from all averaged devices taken for MTF data to give a "true" count value, and therefore modulation factor value.

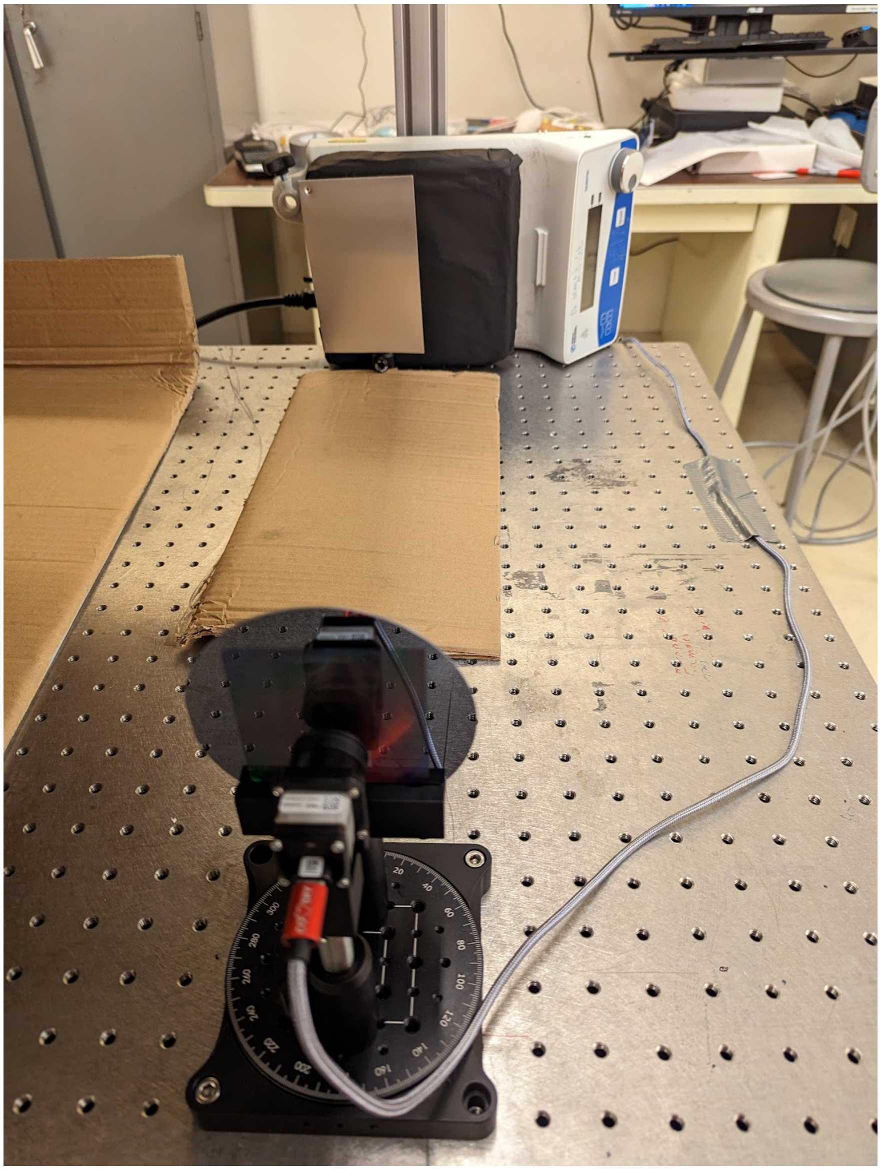

Figure 3.6: Picture of experimental setup. Camera and optic rotate together on stage for MTF measurements, to simulate window being a part of lens optical stack.

3.4.4 MTF difference between system with windows and stock system

To demonstrate that the inset figure shown in Figure 4b of the main text is accurate at nearly all spatial frequencies over all tested field angles, a difference plot is given Figure 3.7. The only exception to this occurs past 34 lp/mm at the 10 degree field angle, at which point our silicon optic performs slightly worse than the stock system. These points account for only 3% of those plotted. We note that the plots in Figure 3.7 are given in absolute % differences, that is, the raw modulation factors subtracted from each other. They are not "percent differences" in the proportional sense.

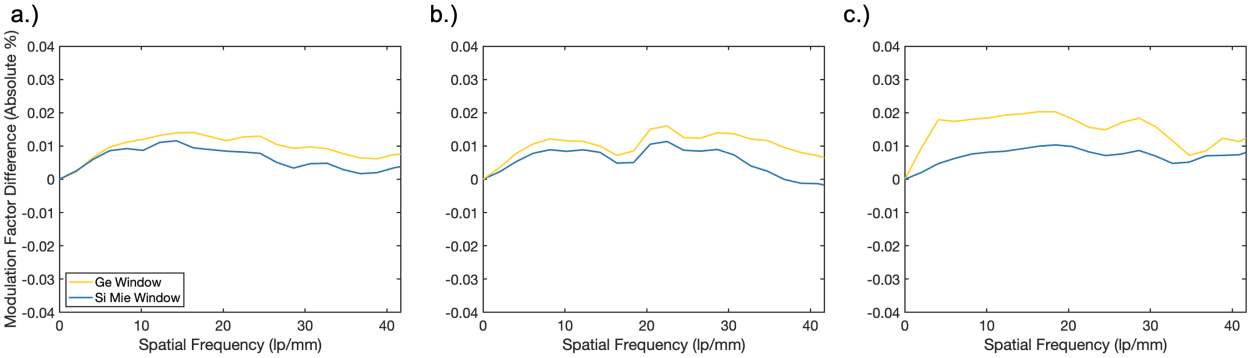

Figure 3.7: Difference between system with added Ge window and stock system (yellow) and system with Si window added and stock system (blue) at each measured spatial frequency a) On axis b.) at 10 degrees and c.) at 14 degrees.

3.4.5 Angular Spectra Comparison

Integrated spectrally averaged transmittance data is shown in the main text to clearly summarize results, but direct comparison of spectra can be seen in Figure 3.8.

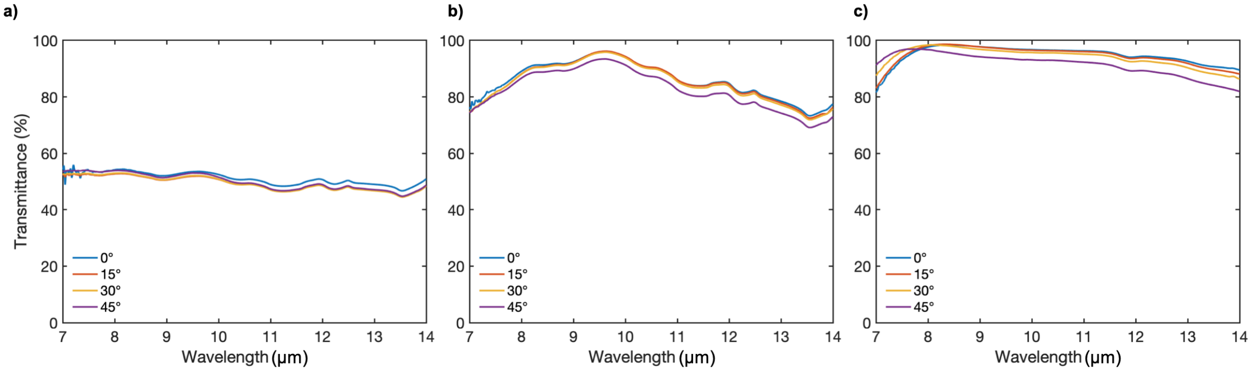

Figure 3.8: Angular spectra measurements for a)bare silicon b)Mie-resonant silicon and c) BBAR coated Germanium window optic.

3.4.6 Front to Back Pattern Misalignment Study

Due to the two-sided nature of the photonic structures, it is reasonable to believe that alignment between the patterning of the two surfaces is an important factor in the performance of the device. Due to the sub-wavelength nature of the features, misalignment generally results in no difference in performance. To confirm this, a series of simulations was run with the Mie-resonant patterns at different percentages out of phase at several incident angles and polarizations, shown in Figure 3.9. They show that at all but the highest angles, alignment of the two surfaces makes no difference. Even at 60°, the divergence seen for any amount of misalignment ends at around 7.5 um. The maximum effect occurs at 7um, which results in transmittance decrease of 7% at that wavelength, tapering off to 0% at 7.5um.

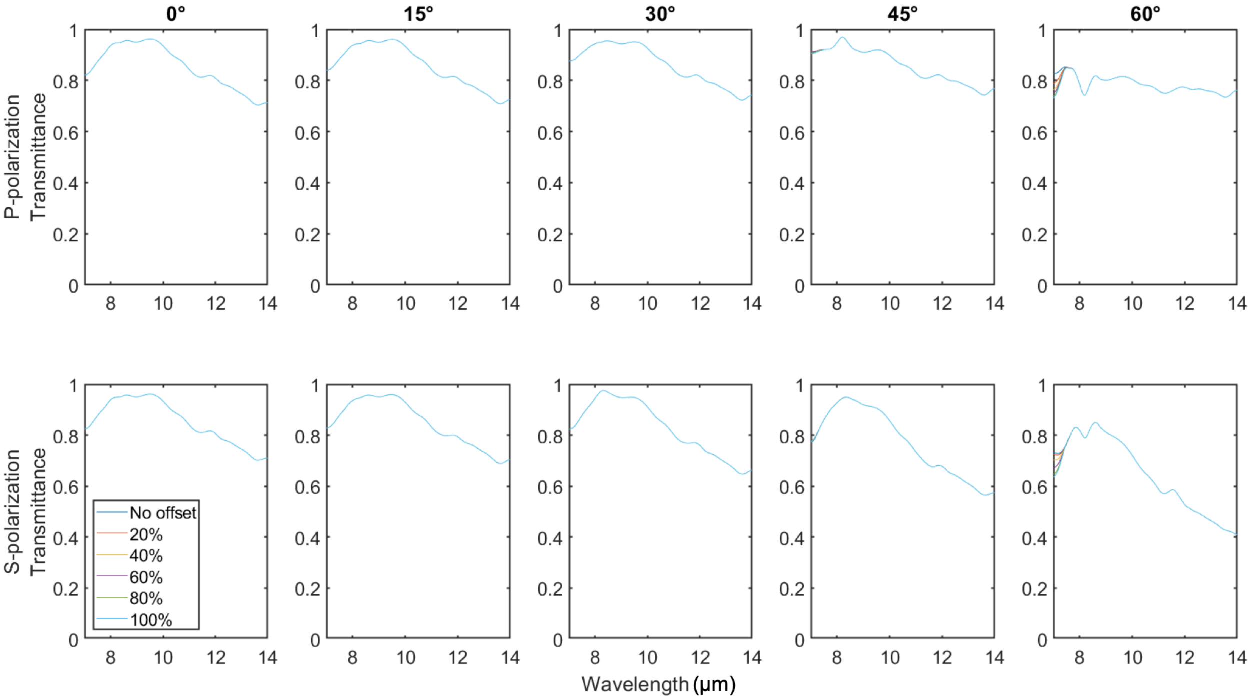

Figure 3.9: Angular spectra measurements for varying degrees of misalignment at 0°, 15°, 30°, 45°, and 60° incidence angles (columns) for S and P polarizations (rows). Note that all lines are overlapping, so only fully out of phase misalignment color is visible. This is confirmed by the 60° simulations, which show slight divergence at low wavelengths.

3.4.7 Qualitative comparison of AR approaches and materials

Below we present two tables qualitatively comparing the approaches and materials we cover within the work. While not meant to be comprehensive, this comparison aims to covers notable aspects of the AR approaches used for a functional window optic.

Table 3.1: A brief qualitative comparison table for the AR approaches covered within the work. Asterisk denotes that under normal conditions adhesion is very good, but large thermal swings can cause delamination, as covered in the main text.

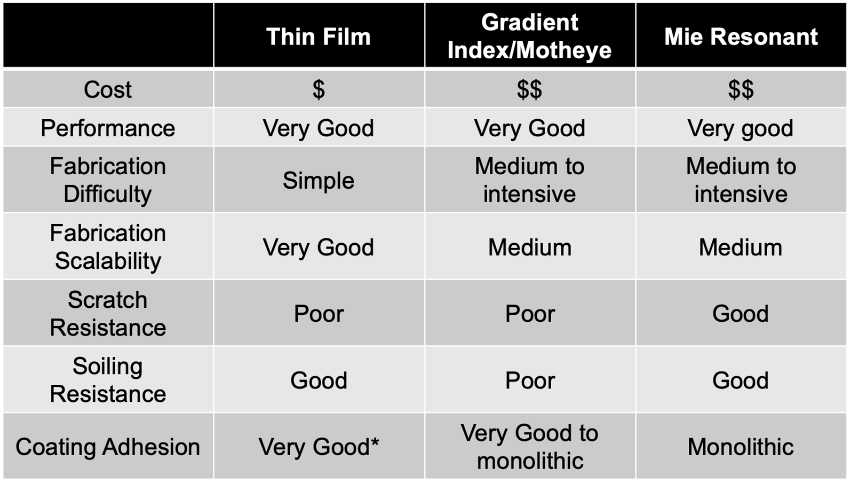

	Thin Film	Gradient Index/Motheye	Mie Resonant
Cost	$	$$	$$
Performance	Very Good	Very Good	Very good
Fabrication Difficulty	Simple	Medium to intensive	Medium to intensive
Fabrication Scalability	Very Good	Medium	Medium
Scratch Resistance	Poor	Poor	Good
Soiling Resistance	Good	Poor	Good
Coating Adhesion	Very Good*	Very Good to monolithic	Monolithic

Table 3.2: A brief qualitative comparison table for the material systems covered within the work.

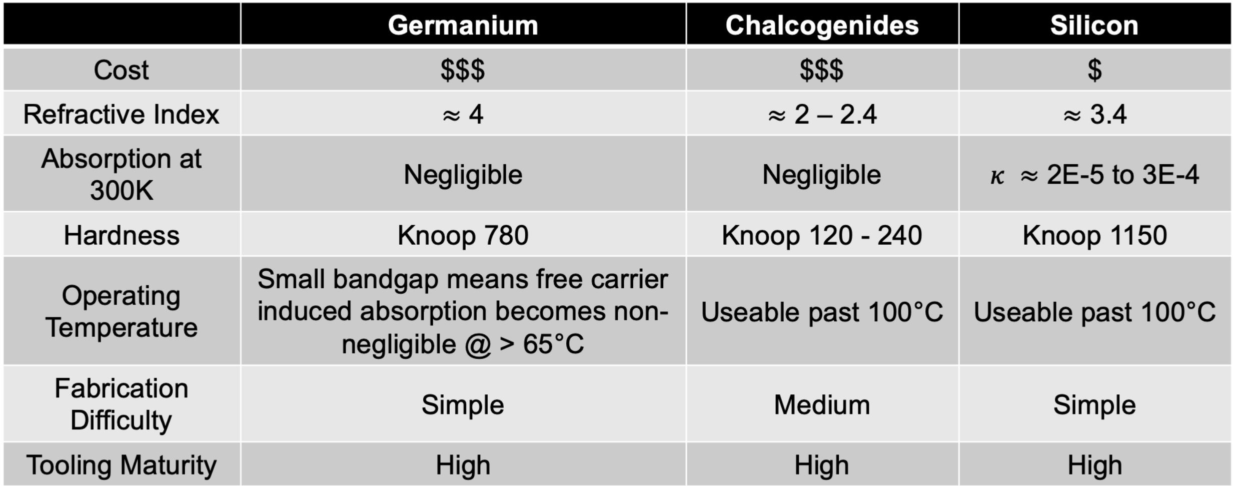

	Germanium	Chalcogenides	Silicon
Cost	$$$	$$$	$
Refractive Index	≈ 4	≈ 2 – 2.4	≈ 3.4
Absorption at 300K	Negligible	Negligible	κ ≈ 2E-5 to 3E-4
Hardness	Knoop 780	Knoop 120 - 240	Knoop 1150
Operating Temperature	Small bandgap means free carrier induced absorption becomes non-negligible @ > 65°C	Useable past 100°C	Useable past 100°C
Fabrication Difficulty	Simple	Medium	Simple
Tooling Maturity	High	High	High

3.4.8 Acknowledgement

This material is based upon work supported by the National Science Foundation (NSF CAREER) under Grant No. 2146577, the DARPA Young Faculty Award (W911NF2110345), and the Sloan Research Fellowship (Alfred P. Sloan Foundation). J.B. was supported by a National Science Foundation Graduate Research Fellowship under grants DGE-1650605 and DGE-2034835, as well as the NSF funded UCLA NRT-INFEWS Program under grant number (INFEWS)-DGE-1735325. Additionally, this work used computational and storage services associated with the Hoffman2 Shared Cluster provided by UCLA Office of Advanced Research Computing's Research Technology Group. Fabrication of the devices shown in this work was done in the UCLA Nanolab Nanoelectronics Research Facility.

CHAPTER 4

Resonant surface engineering for photovoltaic cell front glass improvement

4.1 Background

As of 2021, photovoltaic cells are the largest sources of renewable energy on earth, with an estimated 1032.5 TWh generated, and making up over 50% of all currently generated renewable energy[132]. As demand for photovoltaic cells continues to increase, enhancing cell and module level efficiency and longevity will be an ongoing pursuit for researchers worldwide.

Many previous approaches to efficiency increases have focused on suppressing reflection more generally, with no regard for which wavelengths are allowed to pass[133,134]. While these solutions seem useful in theory, there are several effects which can increase or lower overall cell efficiency. One key aspect of efficiency is cell operating temperature[135,136]. While cells are conventionally rated for generation at an operating temperature of $25°C$, in general, most cells operate at significantly higher temperatures depending on the climate where they are installed[137]. Sustained lowered cell temperatures can result in cell longevity increases, with a $1°C$ decrease in temperature correlating to a possible 2 year increase in cell life span[137,138]. On the other hand, higher temperatures result in reduced open circuit cell voltages, resulting in sustained lower efficiencies over their peak generation hours. This voltage reduction is due to a combination of cell bandgap narrowing that occurs as temperature increases, as well as increased phonon based scattering effects that increase recombination processes inside the active region of the cell. Equation 4.1[139] shows this dependence:

$$V_{oc} = E_g/q - (KT/q)ln\left(\frac{I_L h^3 c^2}{2\pi qkTE_G^2}\right) \tag{4.1}$$

Increased cell temperatures can be caused by high ambient air and ground temperatures, but is most strongly due to absorption of unnecessary solar wavelengths. The AM 1.5 solar spectrum contains meaningful energy out to approximately 2.5 μm, and for semiconductor materials some portion of this spectrum is sub-bandgap light, which produce useful photocurrent in a single junction cell. For c-Si cells, making up around 95% of all installed cells worldwide[132], this cutoff occurs at approximately 1.2 μm, with light above these wavelengths only serving to heat the cell module. It should be noted that silicon itself is not strongly absorbing at these wavelengths, but other module components such as the cell encapsulant, contact fingers, and metal frame are. Heating of these module components will result in heating of the silicon through conductive means.

This means that solutions which broadly target anti-reflection of the front glass can actually result in efficiency decreases in practice. Additionally, even those approaches which focus on increasing the absorption efficiency of the active region neglect thermal absorption of other portions of a module. This in turn still results in increased heating and decreased efficiency, even if silicon itself is more efficient. With this in mind, considerable research effort has been invested into effectively lowering cell temperatures[140–143]. Ideally, a holistic approach which considers thermal practicalities while also increasing active region absorption is a necessity to make sustained efficiency gains. Approaches of this type have been investigated in the past[144–146], and resulted in highly performant designs, however these designs involve complex multilayer stacks with over 30 layers.

4.2 Design and Simulation Landscape

With these considerations in mind, we investigate a possible simpler method of module front glass modification that is able to effectively reflect sub-bandgap incidence while maintaining useful transmission to the cell junction. Our proposed design consists of only 2 embedded layers of patterned resonator structures with a lower index Si_3N_4 layer followed by a high index Ta_2O_5 layer. This is then topped with an anti-reflective layer of index optimal silica aerogel. A schematic of our proposed design can be seen in figure 4.1a.

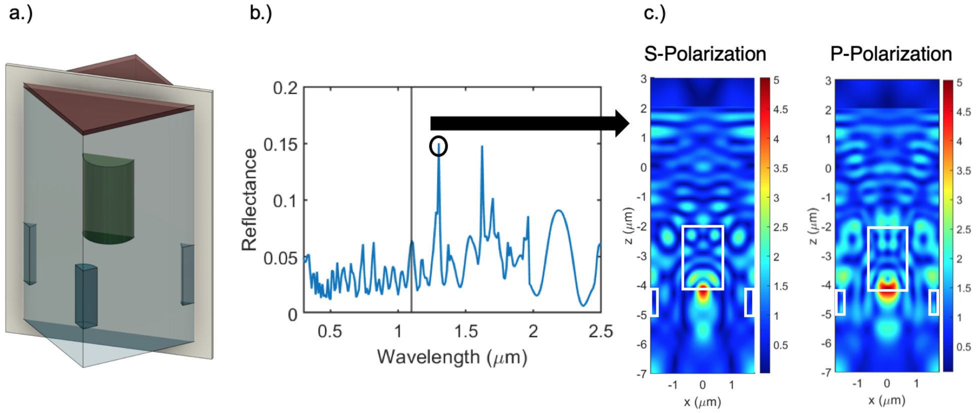

Figure 4.1: a) Pictorial schematic of a single square unit cell cross-section at the top surface of a pane of module glass. Design consists of a silica spacer layer in which is embedded a lower index Si_3N_4 resonator layer followed by a higher index, offset Ta_2O_5 resonator layer, and finally topped with an aerogel anti-reflective layer. b) Simulated performance of optimal design. c) Design E-fields for S and P polarizations, taken at the cross-section shown in a and the peak position noted in b.

This design was arrived at by simulating several different geometries and calculating 2 figures of merit. The visible wavelength merit is given by eq. 4.2 and the sub-bandgap merit is given by 4.3. The design has a 2.5 μm period and consists of a 120 nm aerogel layer, a 3 μm thick spacer layer, a 1.25 μm wide Ta_2O_5 resonator feature with a height of 1.5 μm, and finally a a 1.25 μm laterally offset 250 nm wide TiO_2 resonator feature with a height of 500 nm. It results in an approximately 8 W/m^2 reflected sub-band power, while also slightly improving transmission of useful solar incidence.

$$FOM_{vis} = \int_{0.3\mu m}^{1.1\mu m} SR_{Si}(\lambda) * T(\lambda) d\lambda \tag{4.2}$$

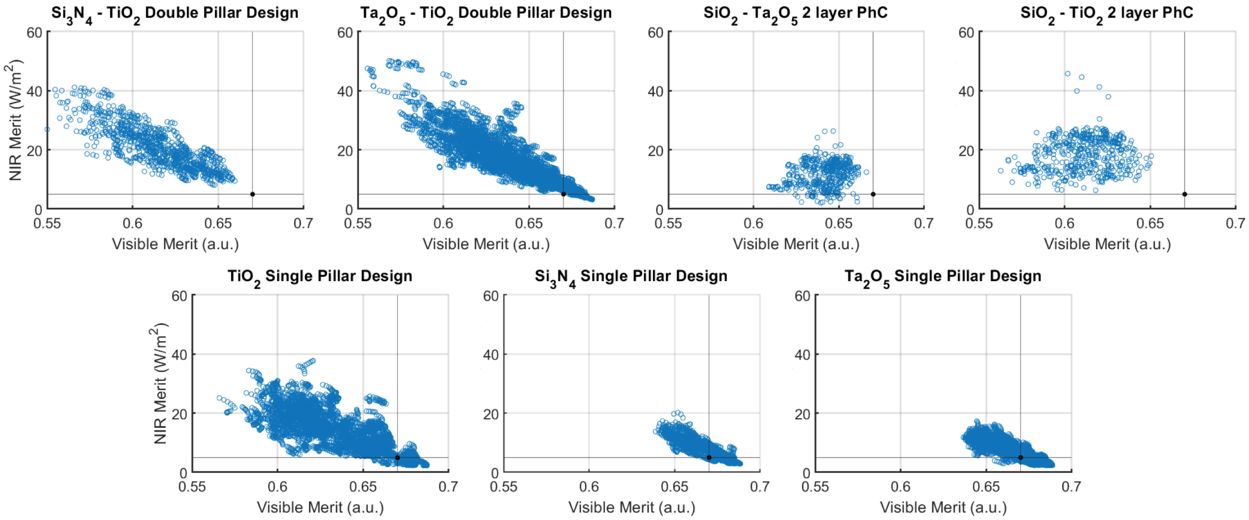

Figure 4.2: Optimization landscape diagrams of seven different design classes. Two layer resonator designs are shown in the top row, while single resonator layer designs are shown in the bottom row. The meaning of the x-axis value is given by eq. 4.2, while the meaning of the y-axis value is given by eq. 4.3. The black point and corresponding vertical and horizontal line mark the merit position of untreated glass. The goal is to isolate designs which fall in the upper right quadrant with respect to this bare glass "origin". Note that the conventional photonic crystal slab (PhC) designs contain no valid solutions in this quadrant.

$$FOM_{nir} = \int_{1.1\mu m}^{2.5\mu m} AM1.5(\lambda) * R(\lambda) d\lambda \tag{4.3}$$

4.3 Fabrication

After finding a set of optimal designs, we aimed to use available materials and tools to demonstrate our principal. As an initial proof of concept, we fabricated a set of simplified designs which showed increased sub-band reflectance. This design consists of only a single layer of Si_3N_4 resonator structures encapsulated in silica and without the AR layer. We used this to demonstrate the attractive sub-band reflectance properties of our approach.

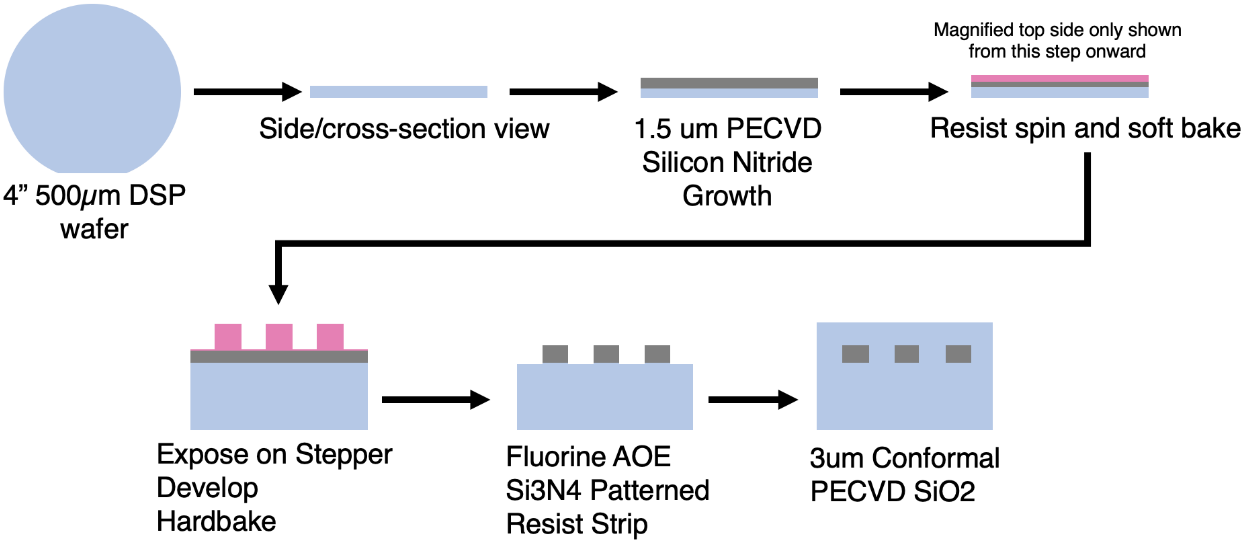
Magnified top side only shown from this step onward
4” 500μm DSP wafer
Side/cross-section view
1.5 um PECVD Silicon Nitride Growth
Resist spin and soft bake
Expose on Stepper
Develop
Hardbake
Fluorine AOE
Si3N4 Patterned
Resist Strip
3um Conformal PECVD SiO2

Figure 4.3: Fabrication outline of patterned glass on fused silica substrate. The final step which was not performed for the initial samples consists of a 120nm aerogel AR coating to assist with visible wavelength transmission efficiency.

The full fabrication process begins with double-side polished fused silica wafers. A 1.5 μm thick layer of Si_3N_4 is deposited on the surface using PECVD, then the wafer follows a standard photolithographic process using a pre-existing mask. This process began with a photoresist coating, followed by exposure on a stepper exposure and alignment tool. This was followed by resist development, which was then etched in a reactive ion etcher using a fluorine based chemistry for design release. After a thorough pirahna cleaning, a final 4.5 μm layer silica layer was deposited on top using PECVD, resulting in a 1.5 μm patterned layer capped by a 3 μm silica spacer layer and completing the optic. A topic for future investigation is the application of a thin ~120 nm aerogel layer for enhanced visible range transmissivity.

The pre-existing mask allowed us to investigate several different design duty cycles and lattice types, but all had a period of 2 μm. 8 designs were investigated, which were composed of a square lattice with a square feature, a square lattice with a circular feature, and a hexagonal lattice with a circular features. The hexagonal lattice and square lattice of square feature designs have 1 of 3 feature spacings of 0.6 μm, 0.5 μm, or 0.35 μm. The square lattice with circular features only included 0.6 μm or 0.5 μm feature spacings, for a total of 8 investigated designs.

4.4 Measurement and Results

The measured sub-band specular reflection data at 10 degree incidence of the patterned samples and bare glass are shown in figure 4.4. We can identify several designs that largely limit influx of sub-band incidence and increase reflection of the front glass signficantly. Measurement was performed with respect to a Au coated reference sample with nearly 100% reflectance over the range from 1.2 - 2.5 μm

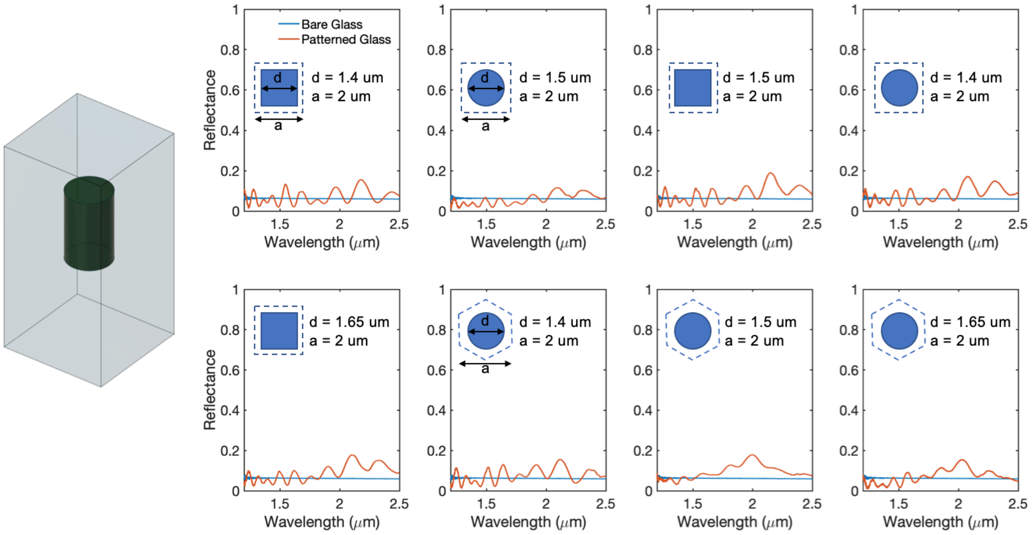

Figure 4.4: a) A representative example design consisting of an Si_3N_4 resonator layer encapsulated in an SiO_2 matrix. Actual resonator cross-section shape is shown in each plot inset, presented with geometric parameters. b) Measured reflectance of 8 proof of concept designs, compared to bare, unpatterned glass.

This comparison makes the possible subband reflective performance advantage apparent. Further tuned approaches with better materials such as Ta_2O_5 hold promise in further optimizing the performance of glass modification with a relatively simple process, and leveraging resonant behaviors. The best proof of concept design (panel 7 of figure 4.4b) shows a $\sim 12\frac{W}{m^2}$ AM1.5 Global weighted NIR integrated reflectance from 1.2 to 2.5 μm.

In conclusion, I show how a resonant patterning approach can be used to in order to increase sub-band reflectivity of module front glass panels. This approach is in theory able to perform this without affecting and even increasing useful transmitted energy into the active region of the solar cell. Initial experimental realizations demonstrate the subband filtering function of this class of designs even under poorly optimized conditions, and pave the way for future designs with significantly better performance when well optimized and aerogel coated.

CHAPTER 5

Conclusions and Future Work

While thermal optics is a healthy field, possibilities for innovations abound. The field holds promise in continuing to improve medical technologies, remote sensing, and imaging systems more generally that are not possible using visible wavelength systems. Additionally, for the many devices and studies that do target visible optical regimes, LWIR optics can serve as a useful larger scale test bed to investigate nanophotonics. Work in optical metamaterials and metasurfaces has made current cutting edge microfabrication techniques pivotal to investigating a wide range of phenomena. Unfortunately, technologies such as e-beam based lithography are serial and therefore inherently unscalable, making visible wavelength investigation limited to small device areas. This places the LWIR wavelengths at an ideal scale for current production of larger area devices investigating metasurfaces and metamaterial based functionality.

In particular, the study of geometry-based resonances in dielectrics, also known as all dielectric Mie-resonances, constitute an active and continuing field of research, due to their attractive tunable responses and extremely low optical losses. More broadly, optical resonances have traditionally be studied for uses targeting narrowband phenomena and extremely high quality factor responses. It is important to stress that while these studies are necessary for optical advancement as a whole, low quality factor, broadband, tunable resonant behavior is also of extreme importance. Natural systems often exhibit broadband characteristics, and control of extant natural EM radiation will continue to become important as humanity searches for new ways to harvest and harness optical and thermal energy. While conventional optical approaches already exist such as spectral filters or interference coatings to enable broadband behavior, the advent of metamaterial systems holds promise in unlocking angle and polarization resolved functionalities, as well as combining multiple functions of previous approaches concurrently.

Bibliography

[1] A. R. Martin and A. H. Jr. Bond. Nuclear pulse propulsion: a historical review of an advanced propulsion concept. *Journal of the British Interplanetary Society*, 32:283, 1979.

[2] Keith A Beals, Martin Beaulieu, Frank J Dembia, Joseph Kerstiens, Daniel L Kramer, Jeffrey R West, and James A Zito. *Project longshot: An unmanned probe to Alpha Centauri*. United States Naval Academy, 1988.

[3] Alan. Bond and Project Daedalus Study Group. *Project Daedalus : The final report on the BIS starship study*. British Interplanetary Society, London, England, 1978.

[4] K.F. Long, R.K. Obousy, and A. Hein. Project icarus: Optimisation of nuclear fusion propulsion for interstellar missions. *Acta Astronautica*, 68(11):1820–1829, 2011.

[5] K. Wagner, A. Boehle, P. Pathak, M. Kasper, R. Arsenault, G. Jakob, U. Käufl, S. Leveratto, A. L. Maire, E. Pantin, R. Siebenmorgen, G. Zins, O. Absil, N. Ageorges, D. Apai, A. Carlotti, Choquet, C. Delacroix, K. Dohlen, P. Duhoux, P. Forsberg, E. Fuenteseca, S. Gutruf, O. Guyon, E. Huby, D. Kampf, M. Karlsson, P. Kervella, J. P. Kirchbauer, P. Klupar, J. Kolb, D. Mawet, M. N'Diaye, G. Orban de Xivry, S. P. Quanz, A. Reutlinger, G. Ruane, M. Riquelme, C. Soenke, M. Sterzik, A. Vigan, and T. de Zeeuw. Imaging low-mass planets within the habitable zone of α Centauri. *Nature Communications*, 12(1):1–7, 2021.

[6] Xavier Dumusque, Francesco Pepe, Christophe Lovis, Damien Ségransan, Johannes Sahlmann, Willy Benz, François Bouchy, Michel Mayor, Didier Queloz, Nuno Santos, and Stéphane Udry. An Earth-mass planet orbiting α Centauri B. *Nature*, 491(7423):207–211, 2012.

[7] Kevin L.G. Parkin. The Breakthrough Starshot system model. *Acta Astronautica*, 152(July):370–384, 2018.

[8] Lukas Novotny and Bert Hecht. *Optical forces*, page 448–473. Cambridge University Press, 2 edition, 2012.

[9] Richard L Garwin. Solar sailing-a practical method of propulsion within the solar system, 1958.

[10] K Eric Drexler. High performance solar sails and related reflecting devices. In *Princeton University and American Institute of Aeronautics and Astronautics, Conference on Space Manufacturing Facilities, 4th, Princeton University, Princeton, N. J*, 1979.

[11] Artur R. Davoyan, Jeremy N. Munday, Nelson Tabiryan, Grover A. Swartzlander, and Les Johnson. Photonic materials for interstellar solar sailing. *Optica*, 8(5):722, 2021.

[12] Y. Tsuda, O. Mori, R. Funase, H. Sawada, T. Yamamoto, T. Saiki, T. Endo, and J. Kawaguchi. Flight status of IKAROS deep space solar sail demonstrator. *Acta Astronautica*, 69(9-10):833–840, 2011.

[13] Manasvi Lingam and Abraham Loeb. Propulsion of spacecraft to relativistic speeds using natural astrophysical sources. *The Astrophysical Journal*, 894(1):36, may 2020.

[14] Matt Wentzel-Long and Geoffrey A Landis. Power generation from interplanetary and interstellar plasma and magnetic fields. *AIAA Propulsion and Energy Forum*, 2020.

[15] Robert L Forward. Roundtrip interstellar travel using laser-pushed lightsails. *Journal of Spacecraft and Rockets*, 21(2):187–195, mar 1984.

[16] Neeraj Kulkarni, Philip Lubin, and Qicheng Zhang. Relativistic spacecraft propelled by directed energy. *The Astronomical Journal*, 155(4):155, mar 2018.

[17] J. L. Redding. Interstellar vehicle propelled by terrestrial laser beam. *Nature*, 213(5076):588–589, 1967.

[18] David Kipping. Relativistic light sails. *The Astronomical Journal*, 153(6):277, 2017.

[19] Harry A. Atwater, Artur R. Davoyan, Ognjen Ilic, Deep Jariwala, Michelle C. Sherrott, Cora M. Went, William S. Whitney, and Joeson Wong. Materials challenges for the Starshot lightsail. *Nature Materials*, 17(10):861–867, 2018.

[20] Matthew F Campbell, John Brewer, Deep Jariwala, Aaswath P Raman, and Igor Bargatin. Relativistic Light Sails Need to Billow. *Nano Letters*, 2022.

[21] Mohammad Mahdi Salary and Hossein Mosallaei. Photonic metasurfaces as relativistic light sails for doppler-broadened stable beam-riding and radiative cooling. *Laser and Photonics Reviews*, 1900311:1–19, 2020.

[22] Zachary Manchester and Abraham Loeb. Stability of a light sail riding on a laser beam. *The Astrophysical Journal*, 837(2):L20, mar 2017.

[23] Thiem Hoang, A. Lazarian, Blakesley Burkhart, and Abraham Loeb. The interaction of relativistic spacecrafts with the interstellar medium. *The Astrophysical Journal*, 837(1):5, feb 2017.

[24] Thiem Hoang and Abraham Loeb. Electromagnetic forces on a relativistic spacecraft in the interstellar medium. *The Astrophysical Journal*, 848(1):31, oct 2017.

[25] James T Early and Richard A London. Dust grain damage to interstellar laser-pushed lightsail. *Journal of Spacecraft and Rockets*, 37(4):526–531, 2000.

[26] Stephen Y Chou, Peter R Krauss, Preston J Renstrom, Stephen Y Chou, Peter R Krauss, and Preston J Renstrom. Imprint lithography with 25-nanometer resolution. *Science*, 272(5258):85–87, 1996.

[27] Yifang Chen. Nanofabrication by electron beam lithography and its applications: A review. *Microelectronic Engineering*, 135:57–72, 2015.

[28] Richard W. Johnson, Adam Hultqvist, and Stacey F. Bent. A brief review of atomic layer deposition: From fundamentals to applications. *Materials Today*, 17(5):236–246, 2014.

[29] Aaswath P Raman, Marc Abou Anoma, Linxiao Zhu, Eden Rephaeli, and Shanhui Fan. Passive radiative cooling below ambient air temperature under direct sunlight. *Nature*, 515:540, nov 2014.

[30] Eden Rephaeli, Aaswath Raman, and Shanhui Fan. Ultrabroadband photonic structures to achieve high-performance daytime radiative cooling. *Nano Letters*, 13(4):1457–1461, 2013.

[31] L. A. Kolodziejski, Shanhui Fan, P. Villeneuve, and J. D. Joannopoulos. Guided modes in photonic crystal slabs. *Physical Review B - Condensed Matter and Materials Physics*, 60(8):5751–5758, 1999.

[32] Shanhui Fan and J. D. Joannopoulos. Analysis of guided resonances in photonic crystal slabs. *Physical Review B - Condensed Matter and Materials Physics*, 65(23):1–8, 2002.

[33] Sean Molesky, Zin Lin, Alexander Y. Piggott, Weiliang Jin, Jelena Vucković, and Alejandro W. Rodriguez. Inverse design in nanophotonics. *Nature Photonics*, 12(11):659–670, 2018.

[34] Nanfang Yu and Federico Capasso. Flat optics with designer metasurfaces. *Nature Materials*, 13(2):139–150, 2014.

[35] Mohammad Mahdi Salary and Hossein Mosallaei. Inverse design of diffractive relativistic meta-sails via multi-objective optimization. *Advanced Theory and Simulations*, 2100047:1–16, 2021.

[36] Ognjen Ilic and Harry A. Atwater. Self-stabilizing photonic levitation and propulsion of nanostructured macroscopic objects. *Nature Photonics*, 13(4):289–295, 2019.

[37] Ognjen Ilic, Cora M. Went, and Harry A. Atwater. Nanophotonic heterostructures for efficient propulsion and radiative cooling of relativistic light sails. *Nano Letters*, 18(9):5583–5589, 2018.

[38] Weiliang Jin, Wei Li, Meir Orenstein, and Shanhui Fan. Inverse design of lightweight broadband reflector for relativistic lightsail propulsion. *ACS Photonics*, 7(9):2350–2355, 2020.

[39] Ramon Gao, Yonghwi Kim, Laura Kim, Michael D. Kelzenberg, Ognjen Ilic, and Harry A. Atwater. Self-stabilizing silicon nitride lightsails. *Conference Proceedings - Lasers and Electro-Optics Society Annual Meeting-LEOS*, 2020-May:4–5, 2020.

[40] Jan M Zazula. On Graphite Transformations at High Temperature and Pressure Induced by Absorption of the LHC Beam. Technical report, CERN, 1997.

[41] Hieu T. Nguyen, Fiacre E. Rougieux, Bernhard Mitchell, and Daniel Macdonald. Temperature dependence of the band-band absorption coefficient in crystalline silicon from photoluminescence. *Journal of Applied Physics*, 115(4), 2014.

[42] Ting Kuo Kang. Evidence for silicon bandgap narrowing in uniaxially strained MOSFETs subjected to tensile and compressive stress. *IEEE Electron Device Letters*, 33(6):770–772, 2012.

[43] Warren B. Jackson, N. M. Johnson, and D. K. Biegelsen. Density of gap states of silicon grain boundaries determined by optical absorption. *Applied Physics Letters*, 43(2):195–197, 1983.

[44] T. Baehr-Jones, M. Hochberg, and A. Scherer. Photodetection in silicon beyond the band edge with surface states. *Optics Express*, 16(3):1659, 2008.

[45] Sylvain G Cloutier, Pavel A Kossyrev, and Jimmy Xu. Optical gain and stimulated

emission in periodic nanopatterned crystalline silicon. *Nature Materials*, 4(12):887–891, 2005.

[46] Kin Fai Mak, Changgu Lee, James Hone, Jie Shan, and Tony F. Heinz. Atomically thin MoS2: A new direct-gap semiconductor. *Physical Review Letters*, 105(13):2–5, 2010.

[47] Th Böker, R. Severin, A. Müller, C. Janowitz, R. Manzke, D. Voß, P. Krüger, A. Mazur, and J. Pollmann. Band structure of MoS2, MoSe2 and a-MoTe2: Angle-resolved photoelectron spectroscopy and ab initio calculations. *Physical Review B - Condensed Matter and Materials Physics*, 64(23):1–11, 2001.

[48] Georgy A. Ermolaev, Yury V. Stebunov, Andrey A. Vyshnevyy, Dmitry E. Tatarkin, Dmitry I. Yakubovsky, Sergey M. Novikov, Denis G. Baranov, Timur Shegai, Alexey Y. Nikitin, Aleksey V. Arsenin, and Valentyn S. Volkov. Broadband optical properties of monolayer and bulk MoS2. *npj 2D Materials and Applications*, 4(1):1–6, 2020.

[49] Dumitru Dumcenco, Dmitry Ovchinnikov, Kolyo Marinov, Predrag Lazić, Marco Gibertini, Nicola Marzari, Oriol Lopez Sanchez, Yen-Cheng Kung, Daria Krasnozhon, Ming-Wei Chen, Simone Bertolazzi, Philippe Gillet, Anna Fontcuberta i Morral, Aleksandra Radenovic, and Andras Kis. Large-area epitaxial monolayer MoS2. *ACS Nano*, 9(4):4611–4620, apr 2015.

[50] Mengge Li, Jiadong Yao, Xiaoxiang Wu, Shucheng Zhang, Boran Xing, Xinyue Niu, Xiaoyuan Yan, Ying Yu, Yali Liu, and Yewu Wang. P-type doping in large-area monolayer MoS2 by chemical vapor deposition. *ACS Applied Materials & Interfaces*, 12(5):6276–6282, feb 2020.

[51] Changbin Nie, Leyong Yu, Xingzhan Wei, Jun Shen, Wenqiang Lu, Weimin Chen, Shuanglong Feng, and Haofei Shi. Ultrafast growth of large-area monolayer MoS2

film via gold foil assistant CVD for a highly sensitive photodetector. *Nanotechnology*, 28(27):275203, jun 2017.

[52] Karthik Vijay Myilswamy, Aravind Krishnan, and Michelle L. Povinelli. Photonic crystal lightsail with nonlinear reflectivity for increased stability. *Optics Express*, 28(6):8223, 2020.

[53] Yoshio Nishi and Robert Doering. *Handbook of semiconductor manufacturing technology*. CRC press, 2000.

[54] William M Haynes. *CRC handbook of chemistry and physics*. CRC press, 2014.

[55] Xingchen Ji, Samantha Roberts, Mateus Corato-Zanarella, and Michal Lipson. Methods to achieve ultra-high quality factor silicon nitride resonators. *APL Photonics*, 6(7), 2021.

[56] Jan Kischkat, Sven Peters, Bernd Gruska, Mykhaylo Semtsiv, Mikaela Chashnikova, Matthias Klinkmüller, Oliana Fedosenko, Stephan MacHulik, Anna Aleksandrova, Gregorii Monastyrskyi, Yuri Flores, and W. Ted Masselink. Mid-infrared optical properties of thin films of aluminum oxide, titanium dioxide, silicon dioxide, aluminum nitride, and silicon nitride. *Applied Optics*, 51(28):6789–6798, 2012.

[57] Keivan Davami, Lin Zhao, Eric Lu, John Cortes, Chen Lin, Drew E. Lilley, Prashant K. Purohit, and Igor Bargatin. Ultralight shape-recovering plate mechanical metamaterials. *Nature Communications*, 6:1–7, 2015.

[58] Gregory R. Holdman, Gabriel R. Jaffe, Min Seok Jang, Demeng Feng, Mikhail A. Kats, and Victor Watson Brar. Thermal runaway of silicon-based laser sails, 2021.

[59] Senlin Cui, Biao Hu, Bin Ouyang, and Dongdong Zhao. Thermodynamic assessment of the Mo-S system and its application in thermal decomposition of MoS2. *Thermochimica Acta*, 660(September 2017):44–55, 2018.

[60] Peter Cannon. Melting point and sublimation of molybdenum disulphide. *Nature*, 183(4675):1612–1613, 1959.

[61] Hsiang Lin Liu, Teng Yang, Jyun Han Chen, Hsiao Wen Chen, Huaihong Guo, Riichiro Saito, Ming Yang Li, and Lain Jong Li. Temperature-dependent optical constants of monolayer MoS 2 , MoSe 2 , WS 2 , and WSe 2 : spectroscopic ellipsometry and first-principles calculations. *Scientific Reports*, 10(1):1–11, 2020.

[62] A. C. Boccara, Warren Jackson, Nabil M. Amer, and D. Fournier. Sensitive photothermal deflection technique for measuring absorption in optically thin media. *Optics Letters*, 6(1):51, 1981.

[63] M. J. Keevers and M. A. Green. Absorption edge of silicon from solar cell spectral response measurements. *Applied Physics Letters*, 174(November 1994):174, 1995.

[64] Drew Edelberg, Daniel Rhodes, Alexander Kerelsky, Bumho Kim, Jue Wang, Amirali Zangiabadi, Chanul Kim, Antony Abhinandan, Jenny Ardelean, Micheal Scully, Declan Scullion, Lior Embon, Rui Zu, Elton J.G. Santos, Luis Balicas, Chris Marianetti, Katayun Barmak, Xiaoyang Zhu, James Hone, and Abhay N. Pasupathy. Approaching the Intrinsic Limit in Transition Metal Diselenides via Point Defect Control. *Nano Letters*, 19(7):4371–4379, 2019.

[65] Vilas Patil, Jihyun Kim, Khushabu Agrawal, Tuson Park, Junsin Yi, Nobuyuki Aoki, Kenji Watanabe, Takashi Taniguchi, and Gil-Ho Kim. High mobility field-effect transistors based on MoS2 crystals grown by the flux method. *Nanotechnology*, 32(32):325603, may 2021.

[66] Xixia Zhang, Fei Lou, Chunlong Li, Xiang Zhang, Ning Jia, Tongtong Yu, Jingliang He, Baitao Zhang, Haibing Xia, Shanpeng Wang, and Xutang Tao. Flux method growth of bulk MoS2 single crystals and their application as a saturable absorber. *CrystEngComm*, 17(21):4026–4032, 2015.

[67] Zongfu Yu, Aaswath Raman, and Shanhui Fan. Fundamental limit of nanophotonic light trapping in solar cells. *Proceedings of the National Academy of Sciences of the United States of America*, 107(41):17491–17496, 2010.

[68] Zongfu Yu, Aaswath Raman, and Shanhui Fan. Thermodynamic upper bound on broadband light coupling with photonic structures. *Physical Review Letters*, 109(17):1–5, 2012.

[69] Victor Liu and Shanhui Fan. S^4 : A free electromagnetic solver for layered periodic structures. *Computer Physics Communications*, 183(10):2233 – 2244, 2012.

[70] Kevin Luke, Yoshitomo Okawachi, Michael R. E. Lamont, Alexander L. Gaeta, and Michal Lipson. Broadband mid-infrared frequency comb generation in a si3n4 microresonator. *Opt. Lett.*, 40(21):4823–4826, Nov 2015.

[71] WK Widger Jr and MP Woodall. Integration of the planck blackbody radiation function. *Bulletin of the American Meteorological Society*, 57(10):1217–1219, 1976.

[72] Antonio Rogalski. *Infrared detectors*. CRC press, 2010.

[73] P. V.Karthik Yadav, Isha Yadav, B. Ajitha, Abraham Rajasekar, Sudha Gupta, and Y. Ashok Kumar Reddy. Advancements of uncooled infrared microbolometer materials: A review. *Sensors and Actuators A: Physical*, 342(February):113611, 2022.

[74] Jerzy A Dobrowolski. Optical properties of films and coatings. In Michael Bass, editor, *Handbook of Optics: Volume IV - Optical Properties of Materials, Nonlinear Optics, Quantum Optics*, chapter 7. McGraw-Hill Education, New York, 3rd edition edition, 2010.

[75] A. Musset and A. Thelen. Iv multilayer antireflection coatings. In E. Wolf, editor, *Progress in Optics*, volume 8 of *Progress in Optics*, pages 201–237. Elsevier, 1970.

[76] Norbert Kaiser and Hans K Pulker. *Optical Interference Coatings*, volume 88 of *Springer Series in Optical Sciences*. Springer, 2013.

[77] Hemant Kumar Raut, V. Anand Ganesh, A. Sreekumaran Nair, and Seeram Ramakrishna. Anti-reflective coatings: A critical, in-depth review. *Energy and Environmental Science*, 4(10):3779–3804, 2011.

[78] H. Ganesha Shanbhogue, C. L. Nagendra, M. N. Annapurna, S. Ajith Kumar, and G. K. M. Thutupalli. Multilayer antireflection coatings for the visible and near-infrared regions. *Applied Optics*, 36(25):6339, 1997.

[79] Haozhu Wang, Zeyu Zheng, Chengang Ji, and L Jay Guo. Automated multi-layer optical design via deep reinforcement learning. *Machine Learning: Science and Technology*, 2(2):025013, 2021.

[80] Mehdi Keshavarz Hedayati and Mady Elbahri. Antireflective coatings: Conventional stacking layers and ultrathin plasmonic metasurfaces, a mini-review. *Materials*, 9(6):497, 2016.

[81] Jaker Hossain, Bipanko Kumar Mondal, Shaikh Khaled Mostaque, Sheikh Rashel Al Ahmed, and Hajime Shirai. Optimization of multilayer anti-reflection coatings for efficient light management of PEDOT:PSS/c-Si heterojunction solar cells. *Materials Research Express*, 7(1):0–9, 2019.

[82] Peter H. Berning. Use of equivalent films in the design of infrared multilayer antireflection coatings. *J. Opt. Soc. Am.*, 52(4):431–436, Apr 1962.

[83] M C Bautista and A Morales. Silica antireflective films on glass produced by the sol–gel method. *Solar Energy Materials and Solar Cells*, 80(2):217–225, 2003.

[84] Norihiro Mizoshita, Masahiko Ishii, Naohiko Kato, and Hiromitsu Tanaka. Hierarchical

Nanoporous Silica Films for Wear Resistant Antireflection Coatings. *ACS Applied Materials & Interfaces*, 7(34):19424–19430, sep 2015.

[85] Yulu Zhang, Chaoxia Zhao, Pingmei Wang, Longqiang Ye, Jianhui Luo, and Bo Jiang. A convenient sol–gel approach to the preparation of nano-porous silica coatings with very low refractive indices. *Chemical Communications*, 50(89):13813–13816, 2014.

[86] D B Mahadik, R V Lakshmi, and Harish C Barshilia. High performance single layer nano-porous antireflection coatings on glass by sol–gel process for solar energy applications. *Solar Energy Materials and Solar Cells*, 140:61–68, 2015.

[87] Jinpei Wang, Hui Zhang, Ling Wang, Ke Yang, Limin Cang, Xiang Liu, and Wei Huang. Highly Stable and Efficient Mesoporous and Hollow Silica Antireflection Coatings for Perovskite Solar Cells. *ACS Applied Energy Materials*, 3(5):4484–4491, may 2020.

[88] Zuyi Zhang. Antireflective film of porous silica. *Journal of the Optical Society of America A*, 39(7):1172–1178, 2022.

[89] Zuyi Zhang. Dust proof properties of spinodal porous surfaces. *Journal of the Optical Society of America A*, 39(5):866–872, 2022.

[90] Yi-Fan Huang, Surojit Chattopadhyay, Yi-Jun Jen, Cheng-Yu Peng, Tze-An Liu, Yu-Kuei Hsu, Ci-Ling Pan, Hung-Chun Lo, Chih-Hsun Hsu, Yuan-Huei Chang, Chih-Shan Lee, Kuei-Hsien Chen, and Li-Chyong Chen. Improved broadband and quasi-omnidirectional anti-reflection properties with biomimetic silicon nanostructures. *Nature Nanotechnology*, 2:770, Dec 2007.

[91] W H Southwell. Gradient-index antireflection coatings. *Optics Letters*, 8(11):584–586, 1983.

[92] Chih Hung Sun, Peng Jiang, and Bin Jiang. Broadband moth-eye antireflection coatings on silicon. *Applied Physics Letters*, 92(6):2006–2009, 2008.

[93] Hao-Chih Yuan, Vernon E Yost, Matthew R Page, Paul Stradins, Daniel L Meier, and Howard M Branz. Efficient black silicon solar cell with a density-graded nanoporous surface: Optical properties, performance limitations, and design rules. *Applied Physics Letters*, 95(12):123501, sep 2009.

[94] Howard M Branz, Vernon E Yost, Scott Ward, Kim M Jones, Bobby To, and Paul Stradins. Nanostructured black silicon and the optical reflectance of graded-density surfaces. *Applied Physics Letters*, 94(23):231121, jun 2009.

[95] Svetoslav Koynov, Martin S Brandt, and Martin Stutzmann. Black nonreflecting silicon surfaces for solar cells. *Applied Physics Letters*, 88(20):203107, may 2006.

[96] Jia Zhu, Zongfu Yu, George F Burkhard, Ching-Mei Hsu, Stephen T Connor, Yueqin Xu, Qi Wang, Michael McGehee, Shanhui Fan, and Yi Cui. Optical Absorption Enhancement in Amorphous Silicon Nanowire and Nanocone Arrays. *Nano Letters*, 9(1):279–282, jan 2009.

[97] Jia Zhu, Ching-Mei Hsu, Zongfu Yu, Shanhui Fan, and Yi Cui. Nanodome Solar Cells with Efficient Light Management and Self-Cleaning. *Nano Letters*, 10(6):1979–1984, jun 2010.

[98] J A Sánchez-Gil and M Nieto-Vesperinas. Light scattering from random rough dielectric surfaces. *Journal of the Optical Society of America A*, 8(8):1270–1286, 1991.

[99] Federico Lora Gonzalez, Daniel E. Morse, and Michael J. Gordon. Importance of diffuse scattering phenomena in moth-eye arrays for broadband infrared applications. *Optics Letters*, 39(1):13, 2014.

[100] Young Jin Yoo, Yeong Jae Kim, So-Young Kim, Jong Heon Lee, Kyujung Kim, Joo Hwan Ko, Ji Won Lee, Byoung Hun Lee, and Young Min Song. Mechanically robust antireflective moth-eye structures with a tailored coating of dielectric materials. *Optical Materials Express*, 9(11):4178, 2019.

[101] Miguel García, Luis Marroyo, Eduardo Lorenzo, and Miguel Pérez. Soiling and other optical losses in solar-tracking PV plants in navarra. *Progress in Photovoltaics: Research and Applications*, 19(2):211–217, mar 2011.

[102] Ali Samet Sarkı n, Nazmi Ekren, and Şafak Sağlam. A review of anti-reflection and self-cleaning coatings on photovoltaic panels. *Solar Energy*, 199:63–73, 2020.

[103] Hao Lu, Rongrong Cai, Li-Zhi Zhang, Lin Lu, and Longfei Zhang. Experimental investigation on deposition reduction of different types of dust on solar PV cells by self-cleaning coatings. *Solar Energy*, 206:365–373, 2020.

[104] K. R. Catchpole and A. Polman. Design principles for particle plasmon enhanced solar cells. *Applied Physics Letters*, 93(19):191113, 2008.

[105] Harry A. Atwater and Albert Polman. Plasmonics for improved photovoltaic devices. *Nature Materials*, 9(3):205–213, 2010.

[106] P. Spinelli, M. Hebbink, R. De Waele, L. Black, F. Lenzmann, and A. Polman. Optical impedance matching using coupled plasmonic nanoparticle arrays. *Nano Letters*, 11(4):1760–1765, 2011.

[107] P. Spinelli, M. A. Verschuuren, and A. Polman. Broadband omnidirectional antireflection coating based on subwavelength surface Mie resonators. *Nature Communications*, 3:692–695, 2012.

[108] Saman Jahani and Zubin Jacob. All-dielectric metamaterials. *Nature Nanotechnology*, 11(1):23–36, 2016.

[109] Yuri Kivshar and Andrey Miroshnichenko. Meta-optics with mie resonances. *Opt. Photon. News*, 28(1):24–31, Jan 2017.

[110] Arseniy I. Kuznetsov, Andrey E. Miroshnichenko, Mark L. Brongersma, Yuri S. Kivshar, and Boris Luk'yanchuk. Optically resonant dielectric nanostructures. *Science*, 354(6314):846, 2016.

[111] Ragip A. Pala, Serkan Butun, Koray Aydin, and Harry A. Atwater. Omnidirectional and broadband absorption enhancement from trapezoidal Mie resonators in semiconductor metasurfaces. *Scientific Reports*, 6(September):1–7, 2016.

[112] J. van de Groep and A. Polman. Designing dielectric resonators on substrates: Combining magnetic and electric resonances. *Optics Express*, 21(22):26285, 2013.

[113] K. V. Baryshnikova, M. I. Petrov, V. E. Babicheva, and P. A. Belov. Plasmonic and silicon spherical nanoparticle antireflective coatings. *Scientific Reports*, 6(March):1–11, 2016.

[114] Ken Xingze Wang, Zongfu Yu, Sunil Sandhu, Victor Liu, and Shanhui Fan. Condition for perfect antireflection by optical resonance at material interface. *Optica*, 1(6):388, 2014.

[115] Emanuele F. Pecora, Andrea Cordaro, Pieter G. Kik, and Mark L. Brongersma. Broadband Antireflection Coatings Employing Multiresonant Dielectric Metasurfaces. *ACS Photonics*, 5(11):4456–4462, nov 2018.

[116] M E Motamedi, W H Southwell, and W J Gunning. Antireflection surfaces in silicon using binary optics technology. *Applied Optics*, 31(22):4371–4376, 1992.

[117] Andrea Cordaro, Jorik Van De Groep, Søren Raza, Emanuele Francesco Pecora, Francesco Priolo, and Mark L. Brongersma. Antireflection High-Index Metasurfaces Combining Mie and Fabry-Pérot Resonances. *ACS Photonics*, 6(2):453–459, 2019.

[118] Deane Chandler-Horowitz and Paul M. Amirtharaj. High-accuracy, midinfrared ($450\ cm^{-1} \leq \omega \leq 4000\ cm^{-1}$) refractive index values of silicon. *Journal of Applied Physics*, 97(12):123526, 2005.

[119] Edward D Palik. *Handbook of Optical Constants of Solids*, volume 1. Academic Press, 1998.

[120] J. Vanhellemont and E. Simoen. Brother Silicon, Sister Germanium. *Journal of The Electrochemical Society*, 154(7):H572, 2007.

[121] E V Yashina. Preparation and Properties of Polycrystalline ZnS for IR Applications. *Inorganic Materials*, 39(7):663–668, 2003.

[122] M Oikkonen, T Tuomi, and M Luomajärvi. Density of ZnS thin films grown by atomic layer epitaxy. *Journal of Applied Physics*, 63(4):1070–1074, feb 1988.

[123] S E Grillo, M Ducarroir, M Nadal, E Tournié, and J-P Faurie. Nanoindentation of Si, GaP, GaAs and ZnSe single crystals. *Journal of Physics D: Applied Physics*, 36(1):L5, 2003.

[124] E. E. Khawaja, S. M.A. Durrani, A. B. Hallak, M. A. Salim, and M. S. Hussain. Density of thin vapour-deposited films of zinc selenide. *Journal of Physics D: Applied Physics*, 27(5):1008–1013, 1994.

[125] I. W. Boyd, T. D. Binnie, J. I.B. Wilson, and M. J. Colles. Absorption of infrared radiation in silicon. *Journal of Applied Physics*, 55(8):3061–3063, 1984.

[126] K A Osmer, C J Pruszynski, and J Richter. High Temperature IR Absorption Of Low Resistivity Germanium. In *Proc.SPIE*, volume 1112, pages 83–93, sep 1989.

[127] Peter D. Burns and Don Williams. Camera resolution and distortion: Advanced edge fitting. *IS and T International Symposium on Electronic Imaging Science and Technology*, page 171, 2018.

[128] J T Cox and G Hass. Antireflection Coatings for Germanium and Silicon in the Infrared*. *Journal of the Optical Society of America*, 48(10):677–680, 1958.

[129] Christian De Vita, Marco Asa, Mikel Azpeitia Urquia, Maria Eloisa Castagna, Claudio Somaschini, Francesco Morichetti, and Andrea Melloni. ZnS antireflection coating for Silicon for MIR - LWIR applications. *IEEE International Conference on Group IV Photonics GFP*, 2021-Decem:1–2, 2021.

[130] Phillip H. Papatzacos, M. Nadeem Akram, Olivier Hector, Frédéric Lemarquis, Antonin Moreau, Julien Lumeau, and Per Ohlckers. Temperature resistant anti-reflective coating on Si-wafer for long-wave infra-red imaging. *Heliyon*, 9(5):e15888, 2023.

[131] Jin Hoon Kim, Hye Jun Kil, Sangjun Lee, Jinwoo Park, and Jin Woo Park. Interfacial Delamination at Multilayer Thin Films in Semiconductor Devices. *ACS Omega*, 7(29):25219–25228, 2022.

[132] Andrea Bett, Bruno Burger, Lorenz Friedrich, Cristoph Kost, Sebastian Nold, Dominik Peper, Simon Philipps, Ralph Preu, Jochen Rentsch, Gerhard Stryi-Hipp, Harry Wirth, and Warner Warmurth. Photovoltaics report. Technical report, Fraunhofer ISE, 2023.

[133] Hyeongsik Park, Myung hun Shin, S M Iftiquar, Shahzada Qamar Hussain, Minkyu Ju, Youngkuk Kim, Eun-Chel Cho, and Junsin Yi. The light-trapping effect in various textured cover glass for enhancing the current density in silicon heterojunction solar cells. *Optics Communications*, 467:125657, 2020.

[134] Xiaolei Luo, Linfeng Lu, Min Yin, Xiaohong Fang, Xiaoyuan Chen, Dongdong Li, Liyou Yang, Gaofei Li, and Jing Ma. Antireflective and self-cleaning glass with robust moth-eye surface nanostructures for photovoltaic utilization. *Materials Research Bulletin*, 109:183–189, 2019.

[135] A D Jones and C P Underwood. A thermal model for photovoltaic systems. *Fuel and Energy Abstracts*, 43(3):199, 2002.

[136] E. Skoplaki and J. A. Palyvos. Operating temperature of photovoltaic modules: A survey of pertinent correlations. *Renewable Energy*, 34(1):23–29, 2009.

[137] Olivier Dupré, Rodolphe Vaillon, and Martin A. Green. *Thermal behavior of photovoltaic devices: Physics and engineering*. Springer, 2016.

[138] Sarah Kurtz, Kent Whitfield, G TamizhMani, Michael Koehl, David Miller, James Joyce, John Wohlgemuth, Nick Bosco, Michael Kempe, and Timothy Zgonena. Evaluation of high-temperature exposure of photovoltaic modules. *Progress in Photovoltaics: Research and Applications*, 19(8):954–965, 2011.

[139] Martin A. Green. General temperature dependence of solar cell performance and implications for device modelling. *Progress in Photovoltaics: Research and Applications*, 11(5):333–340, 2003.

[140] M. Hasanuzzaman, A. B.M.A. Malek, M. M. Islam, A. K. Pandey, and N. A. Rahim. Global advancement of cooling technologies for PV systems: A review. *Solar Energy*, 137:25–45, 2016.

[141] S. Sargunanathan, A. Elango, and S. Tharves Mohideen. Performance enhancement of solar photovoltaic cells using effective cooling methods: A review. *Renewable and Sustainable Energy Reviews*, 64:382–393, 2016.

[142] J. Siecker, K. Kusakana, and B. P. Numbi. A review of solar photovoltaic systems cooling technologies. *Renewable and Sustainable Energy Reviews*, 79(July 2016):192–203, 2017.

[143] A. Shukla, Karunesh Kant, Atul Sharma, and Pascal Henry Biwole. Cooling methodologies of photovoltaic module for enhancing electrical efficiency: A review. *Solar Energy Materials and Solar Cells*, 160(July 2016):275–286, 2017.

[144] Ian M Slauch, Michael G Deceglie, Timothy J Silverman, and Vivian E Ferry. Spectrally Selective Mirrors with Combined Optical and Thermal Benefit for Photovoltaic Module Thermal Management. *ACS Photonics*, 5(4):1528–1538, apr 2018.

[145] Wei Li, Yu Shi, Kaifeng Chen, Linxiao Zhu, and Shanhui Fan. A Comprehensive Photonic Approach for Solar Cell Cooling. *ACS Photonics*, 4(4):774–782, apr 2017.

[146] T J Silverman, M G Deceglie, I Subedi, N J Podraza, I M Slauch, V E Ferry, and I Repins. Reducing Operating Temperature in Photovoltaic Modules. *IEEE Journal of Photovoltaics*, 8(2):532–540, 2018.